Naval Research Laboratory
Washington, DC 20375-5320

NRL/MR/6394--18-9798

Case-Study Inverse Thermal Analyses of Friction Stir Welds Using Numerical-Analytical Basis Functions

Samuel G. Lambrakos

Center for Computational Materials Science
Materials Science and Technology Division

July 31, 2018

REPORT DOCUMENTATION PAGE

Form Approved OMB No. 0704-0188

1. REPORT DATE *(DD-MM-YYYY)*
31-07-2018

2. REPORT TYPE
Memorandum Report

3. DATES COVERED *(From - To)*

4. TITLE AND SUBTITLE
Case-Study Inverse Thermal Analyses of Friction Stir Welds Using Numerical-Analytical Basis Functions

5a. CONTRACT NUMBER

5b. GRANT NUMBER

5c. PROGRAM ELEMENT NUMBER

6. AUTHOR(S)
Samuel G. Lambrakos

5d. PROJECT NUMBER

5e. TASK NUMBER

5f. WORK UNIT NUMBER
63-4995-08

7. PERFORMING ORGANIZATION NAME(S) AND ADDRESS(ES)
Naval Research Laboratory
4555 Overlook Avenue, SW
Washington, DC 20375-5344

8. PERFORMING ORGANIZATION REPORT NUMBER
NRL/MR/6394--18-9798

9. SPONSORING / MONITORING AGENCY NAME(S) AND ADDRESS(ES)
Office of Naval Research
One Liberty Center
875 North Randolph St., Suite 1425
Arlington, VA 22203

10. SPONSOR / MONITOR'S ACRONYM(S)
ONR

11. SPONSOR / MONITOR'S REPORT NUMBER(S)

12. DISTRIBUTION / AVAILABILITY STATEMENT
DISTRIBUTION STATEMENT A: Approved for public release; distribution is unlimited.

13. SUPPLEMENTARY NOTES

14. ABSTRACT
Inverse thermal analyses of friction stir welds are presented using numerical-analytical basis function, equivalent source distributions and temperature-field constraint conditions. Case studies are presented for inverse thermal analyses of AZ31-Mg-Alloy and Ti-6Al-4V friction stir welds using temperature-field constraints.

15. SUBJECT TERMS
Friction Stir Welding   Inverse Thermal Analysis
Numerical-Analytical Basis Functions

16. SECURITY CLASSIFICATION OF: a. REPORT	b. ABSTRACT	c. THIS PAGE	17. LIMITATION OF ABSTRACT	18. NUMBER OF PAGES	19a. NAME OF RESPONSIBLE PERSON / 19b. TELEPHONE NUMBER *(include area code)*
Unclassified Unlimited	Unclassified Unlimited	Unclassified Unlimited	Unclassified Unlimited	42	Samuel G. Lambrakos / (202) 767-2601

Standard Form 298 (Rev. 8-98)
Prescribed by ANSI Std. Z39.18

This page intentionally left blank.

Introduction

Firction stir welding (FSW) ia a solid-state process where temperatures are below melting, and is significant for various applications because of unique weld characteristics [1-3]. FSW entails joining of a workpiece by means of a stirring tool of given geometry, which has specified translational and rotational speeds (see Fig.1) (see references [4-18]). The present study concerns inverse thermal analyses of FSW processes using a methodology formulated in terms of numerical-analytical basis functions, equivalent source distributions and temperaturess field constraints [19]. References [20-32] describe the general problem of inverse thermal analysis. This report describes inverse thermal analyses of AZ31-Mg-Alloy and Ti-6Al-4V FSWs, which can predict temperature histories within a workpiece for the range of process parameters considered [19, 33-40].

The subject areas presented are organized as follows. First, the procedure for inverse thermal analysis of FSWs using generalized numerical-analytical basis functions and equivalent source distributions is discussed. Second, case study inverse thermal analyses of AZ31-Mg-Alloy and Ti-6Al-4V FSWs are presented. Third, discussion is given concerning aspects of the inverse thermal analysis methodology. Finally, a conclusion is given.

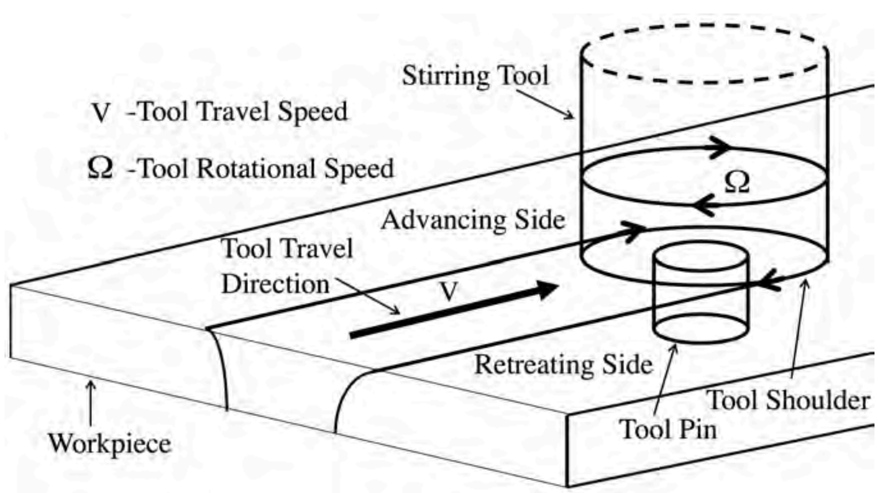

Fig. 1 Schematic representation of friction stir welding and processing.

Manuscript approved July 31, 2018.

Inverse Thermal Analysis Procedure

Following the procedure introduced in [40], the region consisting of stirring tool and stirred material (see Fig. 2) is segmented into a finite set of slices that are perpendicular to the *z* axis. Next, a circle is constructing within each slice , such that the circumference of each circle is defined by the interface between stirred and unstirred material (see Fig. 2). The lines joining centers of these circles and locations of discrete sources, having different strengths, are parallel to V. Accordingly, the *x* and *y* coordinates of each source depends on the width of the stirred-material cross section at its *z* coordinate. This procedure for assigning the locations of discrete sources, of given strengths and diiffusivity vectors $\hat{\kappa}$, permits modeling of asymmetric heat deposition associated with shape differences of FSW advancing and retreating sides.

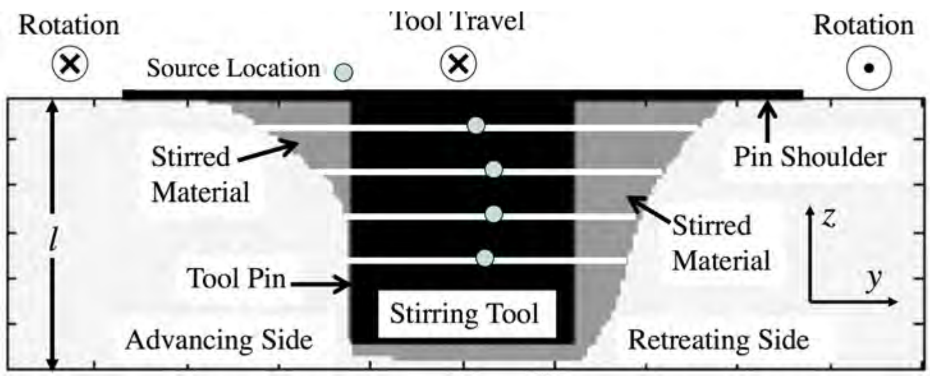

Fig. 2 Schematic representation of FSW cross section consisting of stirring tool and stirred material, where equivalent source distribution consists of point sources located at centers of circles whose diameters are the SZ width as a function of *z*.

Next, a parametric representation of temperature fields for heat deposition during welding of plate structures is adopted, which is terms of an effectively complete set of basis functions. A numerical-analytical basis function whose formulation should be relatively optimal for parametric representation of FSWs is given by

$$T(\hat{x}) = T_A + \sum_{k=1}^{N_k} \frac{C(\hat{x}_k)}{r} \exp\left[-\frac{V}{2\kappa}(r + x - x_k)\right]\left(\sum_{n=1}^{N_t} G(z, z_k, n\Delta t, \kappa)\right) \quad \text{(Eq 1)}$$

and $$T(\hat{x}_n^c, t_n^c) = T_n^c\,,\qquad \text{(Eq 2)}$$

where

$$G(z, z_k, t, \gamma\kappa) = \left\{1 + 2\sum_{m=1}^{\infty} \exp\left[-\frac{(\gamma\kappa)m^2\pi^2 t}{l^2}\right]\cos\left[\frac{m\pi z}{l}\right]\cos\left[\frac{m\pi z_k}{l}\right]\right\} \qquad \text{(Eq 3)}$$

$$r = \sqrt{(x - x_k)^2 + (y - y_k)^2} \qquad \text{(Eq 4)}$$

and

$$C(\hat{x}) = \sum_{k=1}^{N_k} C(\hat{x}_k)\delta(\hat{x} - \hat{x}_k) \qquad \text{(Eq 5)}$$

and where $C(\hat{x}_k)$ is the value of the discrete source function at location $\hat{x}_k$. Equation (1) is the solution to the heat conduction equation for a point source located at position (x_k, y_k, z_k) within a region having non-conducting boundaries in *z*. Specifically, Eq.(1) is constructed using combinations of two general forms of the solution to the heat conduction equation. These general forms are the heat-kernel solution of the time-independent steaty-state heat conduction equation for an unbounded region, and the Fourier series solution of the time-dependent heat conduction equation for a region having non-conduction boundaries. Derivation of these solutions are given in Reference [41]. Equation (5) is the source term of the heat conduction equation associated with a spatial distribution of point sources, which results in the solution given by Eq, (1). The quantities κ, *V*, *l* and γ are the thermal diffusivity, welding speed and workpiece thickness and weight coefficent for modeling equivalent effective-diffusion (associated with equivalent source distributions [40]), respectively. The constraint conditions defined by Eq.(2), representing input quantities to the model, are imposed on the temperature field by minimization of the objective function defined by

$$Z_T = \sum_{n=1}^{N} w_n\left(T(\hat{x}_n^c, t_n^c) - T_n^c\right)^2 \qquad \text{(Eq 6)}$$

where T_n^c is the target temperature for position $\hat{x}_n^c = (x_n^c, y_n^c, z_n^c)$. The quantities w_n (*n=1,…,N*) are weight coefficients specifying relative levels of influence associated with constraint conditions T_n^c. The output quantity of the parametric model defined by Eqs.(1)-(6) is the three-diemsional temperature field $T(\hat{x},t)$ spanning the entire volume of the workpiece. Specifically, the quantitiies $C(\hat{x}_k)$ are adjusted such that temperature-field values calculated according to Eq.(1) are within a small error tolerances of target temperatures at specified positions (see Tables 1). For the present study, conditions on the objective function defined by Eq.(6) were $w_n = 1$ and $\sqrt{Z_T} < 1$ °C, for all *n*. The parameter γ, defined by Eq.(3), implies a diffusivity vector $\hat{\kappa} = (\kappa, \kappa, \gamma\kappa)$ for the equivalent effective-diffusion, and provides convenient adjustment of the temperature field within upstream regions of FSWs that satisfy boundary conditions defined by the SZ, as well as downstream conditions that are determined only by the diffusivity κ (not κ and $\gamma\kappa$). This follows from the mathematical property of heat diffusion within plate structures (see reference [40] for discussion).

The procedure for inverse thermal analysis defined by Eqs.(1)-(6) entails adjustment of parameters $C(\hat{x}_k)$, $\hat{x}_k$, Δt and γ. The parametric model combines numerical integration with optimization of linear combinations of numerical-analytical basis functions, which include fundamental solutions to the heat conduction equation and their Fourier-series representation [41]. Equation (1) defines a discrete numerical integration over time, where the time step Δt is specified according to the average energy per length deposited, for transition of the temperature field, at steady state, from uptream regions (close to the SZ) to downstream regions where there is no longer a *z*-coordinate dependence. It should be noted that the formulation of the inverse analysis methodology defined by Eq.(1)-(6) is equipped with a mathematical structure that satisfies all boundary conditions associated with welding of plate structures (see [19]).

Case Study Inverse Thermal Analysis of AZ31-Mg-Alloy FSWs

In this section results of inverse thermal analyses of AZ31-Mg-Alloy FSWs are described, which correspond to different weld process conditions and associated process-control parameters. AZ31-Mg-Alloy is commercially available in sheet form and offers good mechanical properties, but has limited ductility and tends to be brittle at room temperature. It has been shown, however, that it is possible to form AZ31 sheets having improved ductility and conformability using FS processing, which modifies microstructure [42-50].

The significance of the inverse-problem approach for thermal analysis of FSWs, as for thermal analysis of different types of complex welding processes [19], is that the nature of the energy-source coupling to the workpiece, which is a function of tool geometry and process control parameters, is in principle difficult to specify relative to analysis based on the direct-problem approach. For this study, motivation for adopting SZ boundaries as constraint conditions is that for AZ31-Mg-Alloy FSWs one can associate (approximately) this boundary with an isothermal boundary of known temperature. In the case of the AZ31 magnesium alloy, reference [47] provides an empirical relationship for the estimated uniform SZ temperature as a function of FSW process parameters, which is

$$\frac{T}{T_m} = K\left(\frac{\Omega^2}{V \times 10^4}\right)^{\alpha} \qquad \text{(Eq. 7)}$$

where α = 0.0442, K = 0.8052 and T_m = 610 ^{o}C. The present study uses experimentally estimated SZ boundaries as measured in the laboratory for assigning volumetric constraints (see Eq. (2)) on the calculated temperature fields.

The analyses presented here entail calculation of the steady state temperature field for different shapes of the SZ, which are based on experimentally observed estimates of SZ boundaries. The shapes of these boundaries are determined experimentally by analysis of transverse FSW cross sections showing microstructure revealing estimated SZ boundaries, e.g., see references [46,49,50]. For calculations of the temperature field, which adopt SZ boundaries as constraints, the parameter values assumed are the SZ-edge temperature (T_{sz} determined by Eq.(7)), κ = 4.858 x 10^{-5} m^{2}s^{-1} and Δt = 0.5 s. The diffusivity weight-factor γ, for representation of advective influences (see [40]) is adjusted according to the location of the pseeudo-nonconducting boundary. As discussed previously [37-39], reasonable estimates of κ and isothermal surfaces adopted as field constraints, e.g., SZ-edge temperature T_{sz}, are sufficient for inverse analysis. This follows in that the parameters $C(\hat{x}_k)$, $k=1,...,N_k$, and κ, as well as Δt and γ, are in principle not uniquely determined by inverse analysis. Accordingly, different estimated values of κ, and assigned values of phenomenological parameters Δt and γ, require different values of $C(\hat{x}_k)$ in order to satisfy specified constraint conditions associated with a given isothermal surface.

One goal of the present analysis is determination of parameters that can serve as initial estimates for parameter adjustment with respect to AZ31-Mg-Alloy FSWs, whose process parameters are within similar regimes. Parameter adjustment with respect to other FSWs, which assume the results of this study as initial estimates, would adopt κ and T_{sz} as adjustable parameters, as well as the parameters $C(\hat{x}_k)$, Δt, γ and l_{nc}. Another goal of the present analysis of AZ31-Mg-Alloy FSWs is to provide prototype analyses for demonstrating extension of the methodology for application to FSW analysis in general.

Figures 3 through 8 show estimated transverse cross sections of SZ boundaries for AZ31-Mg-Alloy FSWs obtained from experiment [50] and different two-dimensional slices of three-dimensional temperature fields (°C) calculated using cross section information given in Table 1. Values of the workpiece thickness l and welding speed V for each FSW considered for analysis are given in these figures. The upstream boundary constraints on the temperature field, $T_c = T_{sz}$ for (y_c,z_c) defined in Eq. (2), are given in Table 1 for the SZ boundaries. These constraints are obtained using the estimated transverse weld cross sections of SZ boundaries shown in figures below for the corresponding FSWs, i.e., Welds 1 and 2 . The FSW process parameters resulting in these cross sections are given in these figures.

Given in Tables 2 and 3 are values of the discrete source function that have been calculated according to the constraint conditions given in Table 1. Also indicated in Tables 2 and 3 are the assigned values of parameters Δt, γ and l. With respect to inverse thermal analysis, the constraint conditions given in Table 1 represent target values of temperature for objective function minimization, which were obtained by a distributed sampling of estimated SZ cross sections as measured in the laboratory (see Figs. 3 and 6). The relative location of each discrete source is specified following the procedure for constructing equivalent source distributions, consistent with FSW processes, that is described above. Figures 4, 5, 7 and 8 show different planer slices of steady state temperature fields that have been calculated according to the constraint conditions given in Table 1 for estimated SZ-edge boundaries. Referring to the planar slices of the calculated temperature fields shown in these figures, it should be noted that all constraint and boundary conditions are satisfied, namely the condition $T(\hat{x},t) = T_{sz}$ at the SZ edge, and $\nabla T \cdot \hat{n} = 0$ at workpiece surface boundaries, where $\hat{n}$ is normal to the surface. As shown in these figures, the calculated temperature fields have good agreement with experimentally measured cross sections for SZ-edge boundaries. This agreement does not represent model verification in the same sense as models based on first principles, but rather demonstrates parameter optimization with respect to a given upstream isothermal boundary and workpiece boundary conditions.

Table 1 Estimated SZ-edge boundaries on transverse cross sections of Welds 1 and 2.

WELDS 1 AND 2
(z_c mm, half width mm)
(0.08, 4.48)
(0.4, 3.4)
(0.8, 2.64)
(1.2, 2.0)
(1.6, 1.56)
(2.0, 1.24)

Table 2 Volumetric source function $C(\hat{x}_k)$ calculated according to SZ-boundary constraint conditions given in Table 1, where γ = 0.00605, l = 2.0 mm, Δl = (2.0/60) mm, $x_k = y_k$ = 0.0 for k = 1 to 5 (Weld 1).

k	$C(\hat{x}_k)$ /(1.0x10^{-4})	z_k (Δl)
1	6.2	1
2	0.5	25
3	0.5	30
4	0.5	35
5	0.5	40

Table 3 Volumetric source function $C(\hat{x}_k)$ calculated according to SZ-boundary constraint conditions given in Table 1, where γ = 0.00605, l = 2.0 mm, Δl = (2.0/60) mm, $x_k = y_k$ = 0.0 for k = 1 to 5 (Weld 2).

k	$C(\hat{x}_k)$/(1x10^{-4})	z_k (Δl)
1	5.9	1
2	0.5	25
3	0.5	30
4	0.5	34
5	0.5	40

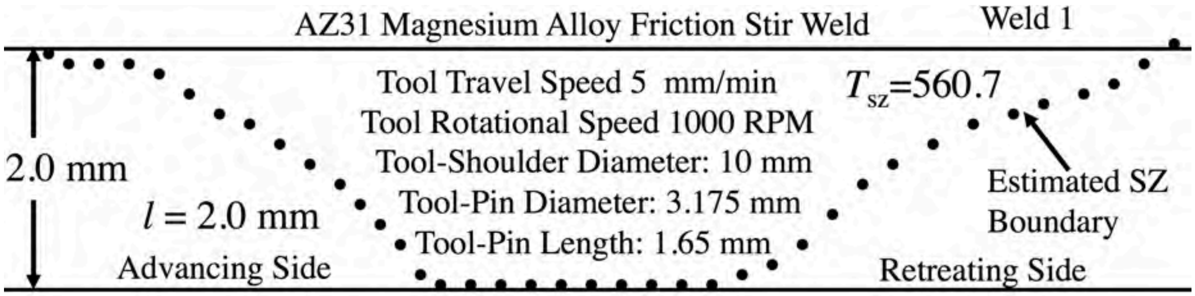

Fig. 3 Experimentally estimated transverse weld cross section of SZ boundary for AZ31-Mg-Alloy FSW [50] (Weld 1).

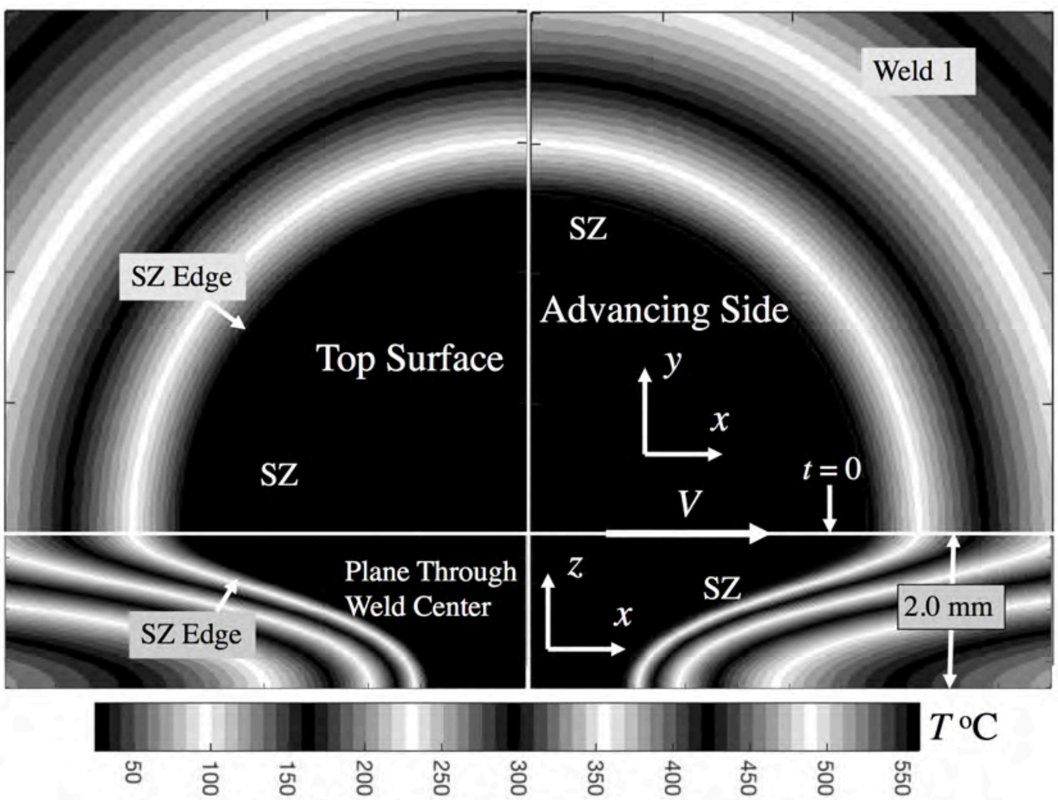

Fig. 4 Two-dimensional slices, at half workpiece top surface and longitudinal cross section at symmetry plane, of three-dimensional temperature field (°C) and isothermal boundary at SZ edge calculated using cross section information given in Table 1, where time = x/V and V = 5 mm/min (Weld 1).

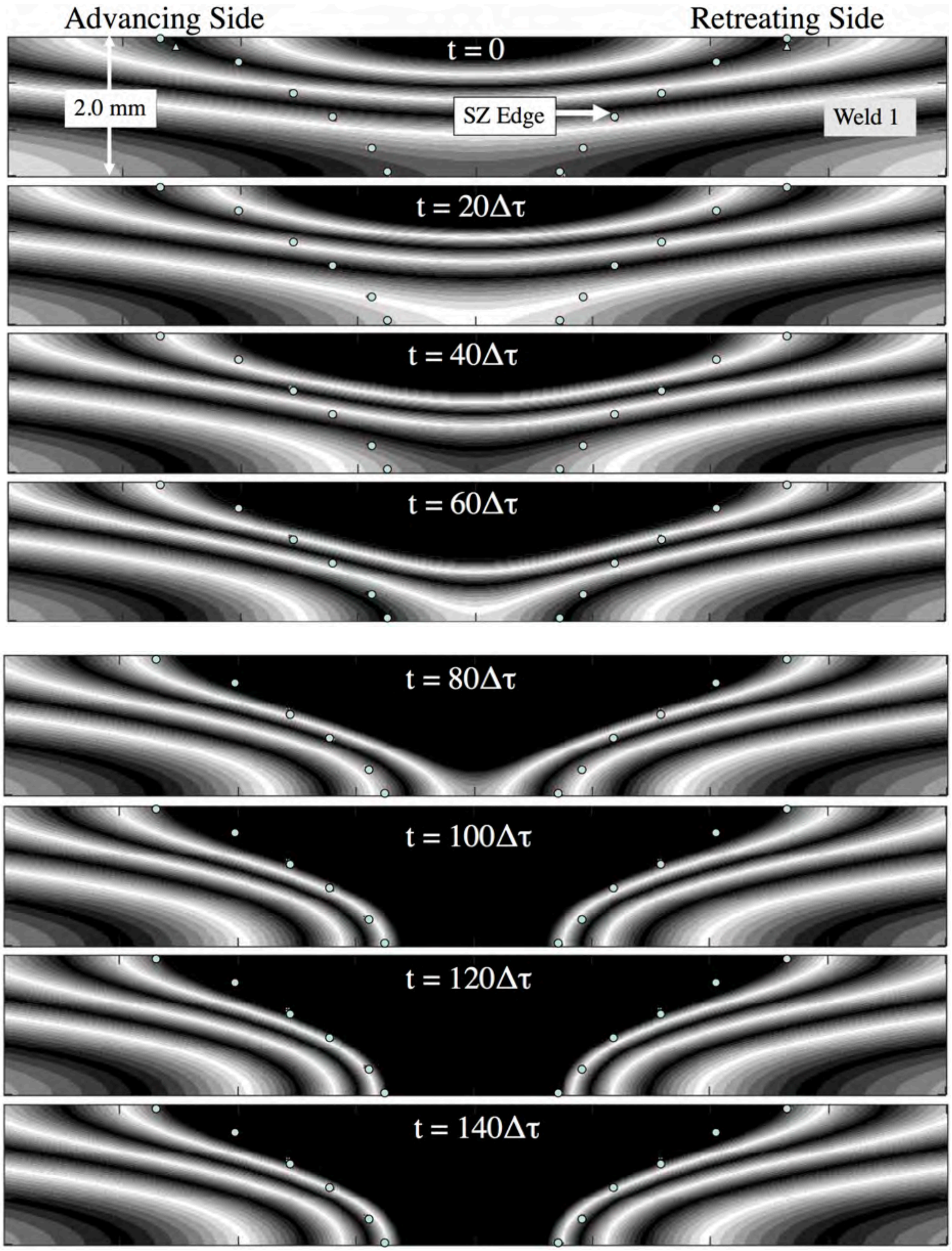

Advancing Side
Retreating Side
t = 0
2.0 mm
SZ Edge
Weld 1
t = 20Δτ
t = 40Δτ
t = 60Δτ
t = 80Δτ
t = 100Δτ
t = 120Δτ
t = 140Δτ

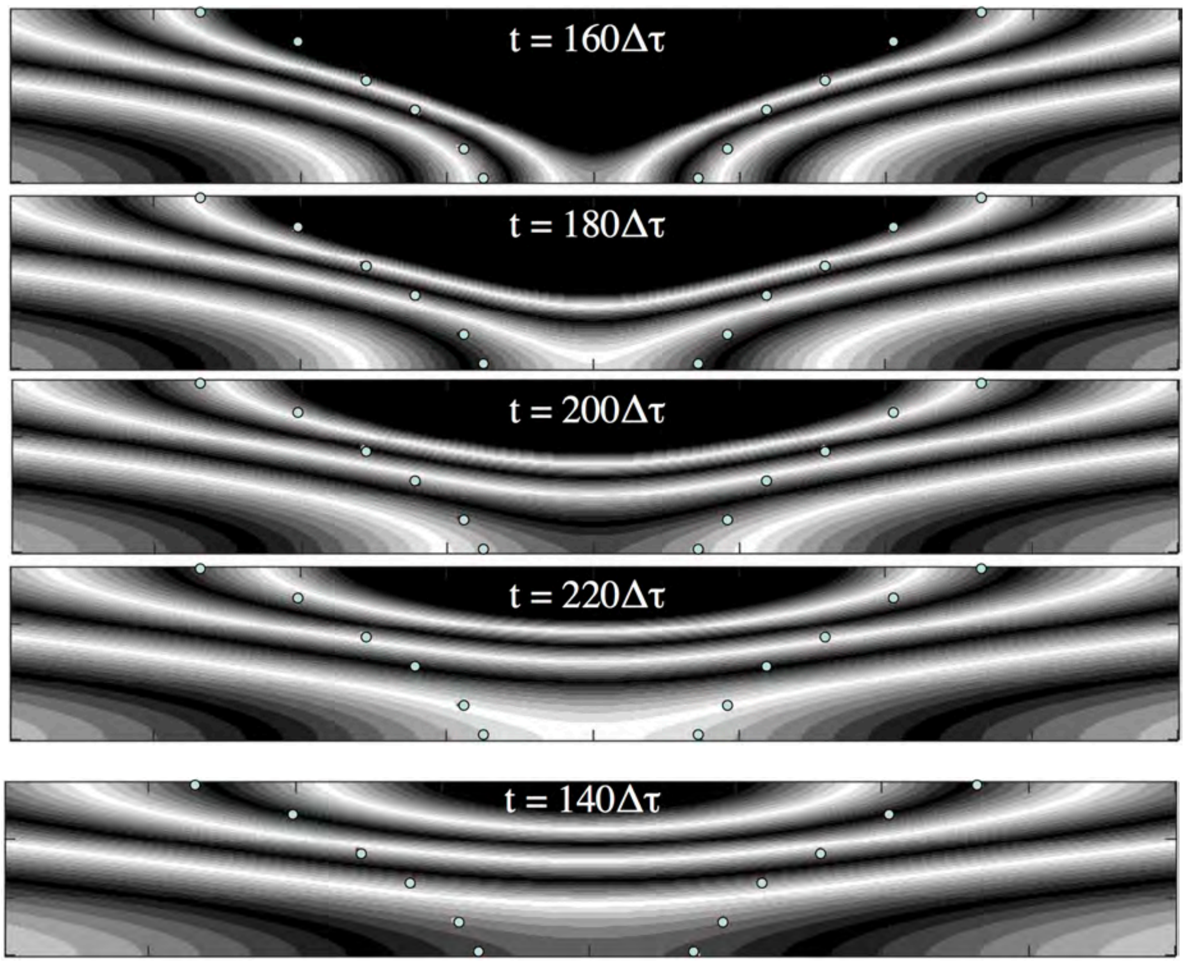

Fig. 5 Temperature history (°C) of transverse cross section of weld calculated using SZ cross-section constraints given in Table 1, where $\Delta\tau = \Delta l / V$, Δl = (3.0/60) mm and V = 5 mm/min (Weld 1). Temperature scale and time origin t = 0 are shown in Fig. 4.

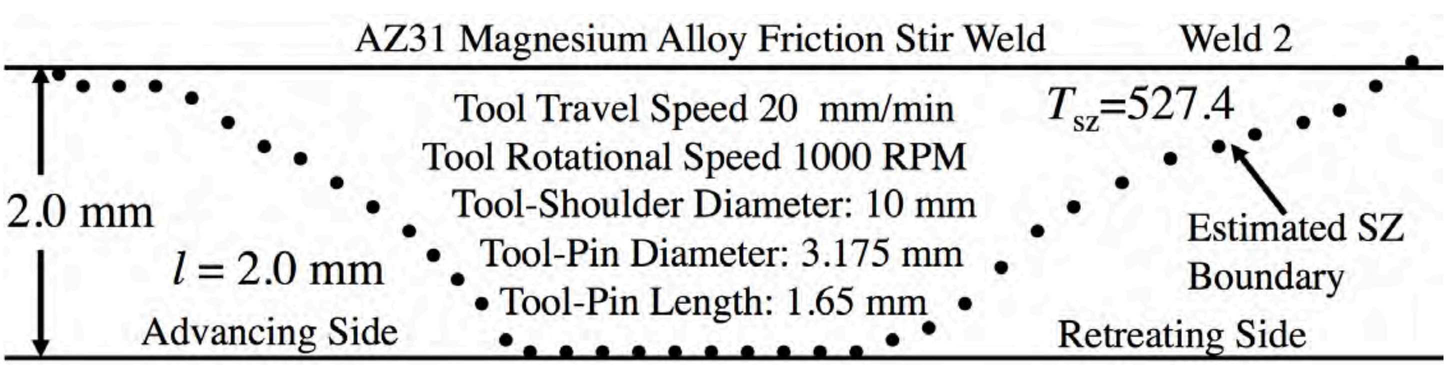

Fig. 6 Experimentally estimated transverse weld cross section of SZ boundary for AZ31-Mg-Alloy FSW [50] (Weld 2).

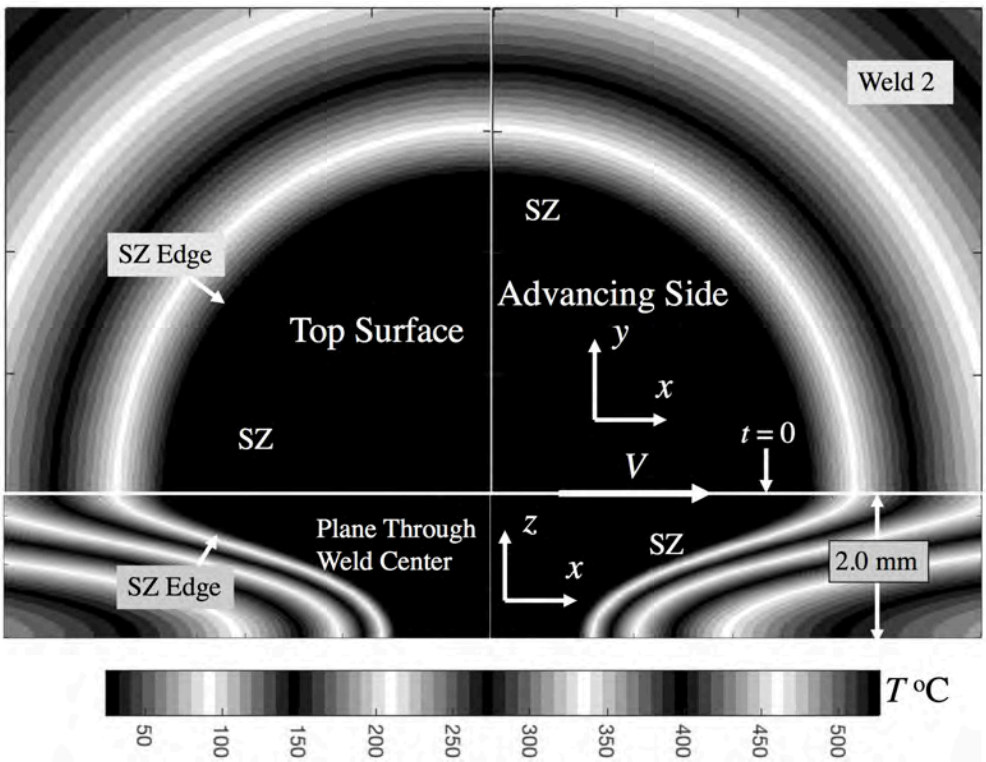

Fig. 7 Two-dimensional slices, at half workpiece top surface and longitudinal cross section at symmetry plane, of three-dimensional temperature field (°C) and isothermal boundary at SZ edge calculated using cross section information given in Table 1, where time = *x*/V and V = 20 mm/min (Weld 2).

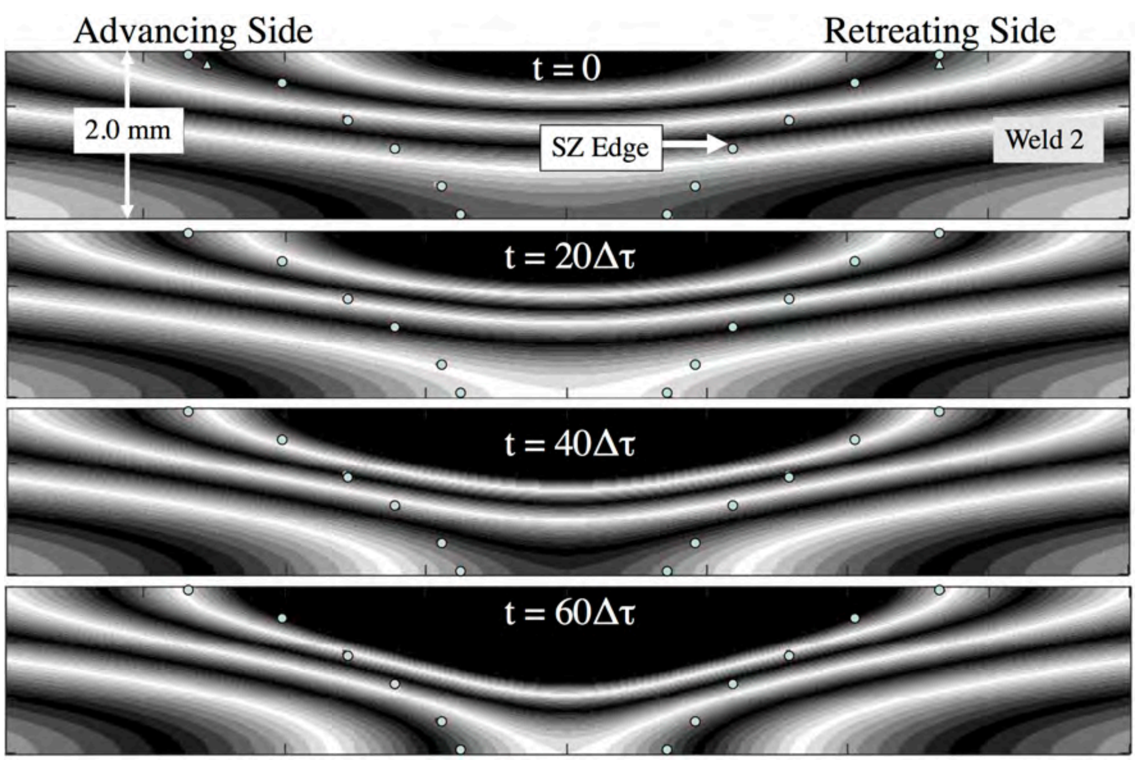

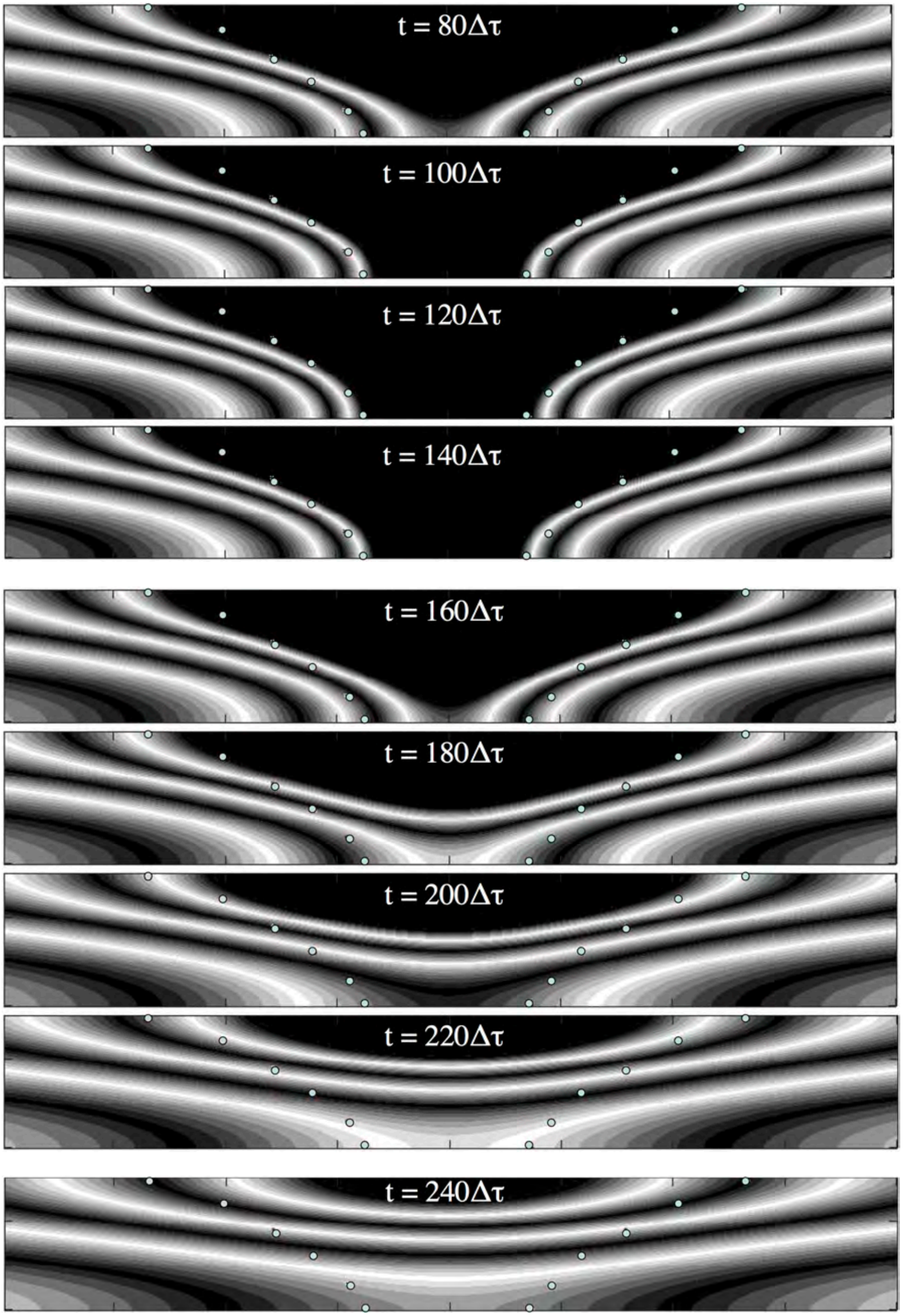
t = 80Δτ
t = 100Δτ
t = 120Δτ
t = 140Δτ
t = 160Δτ
t = 180Δτ
t = 200Δτ
t = 220Δτ
t = 240Δτ

Fig. 8 Temperature history (°C) of transverse cross section of weld calculated using SZ cross-section constraints given in Table 1, where $\Delta\tau = \Delta l/V$, Δl = (2.0/60) mm and V = 20 mm/min (Weld 2). Temperature scale and time origin t = 0 are shown in Fig. 7.

Case Study Inverse Thermal Analysis of Ti-6Al-4V FSWs

In this section results of inverse thermal analyses of Ti-6Al-4V FSWs are described, which correspond to different weld process conditions and associated process-control parameters. For this study, motivation for adopting $\alpha-\beta$ phase transformation boundaries as constraint conditions is that in practice, for welds of Ti and its alloys, one can associate (approximately) this boundary with the observed edge of the HAZ, and accordingly, specify an isothermal boundary of known temperature. The present study uses experimentally estimated HAZ-edge boundaries as measured in the laboratory for assigning volumetric constraints (see Eq.(2)) on the calculated temperature fields.

The analyses presented here entail calculation of the steady state temperature field for different shapes of SZ boundaries within the neighborhood of the stirring tool boundary, and experimentally observed estimates of the HAZ edge. The shapes of these boundaries are determined experimentally by analysis of transverse weld cross sections showing microstructure revealing estimated SZ and HAZ-edge boundaries (see reference [51]). For calculations of the temperature field, adopting HAZ-edge boundaries as constraints, parameter values assumed are $\kappa = 8.6 \times 10^{-6}$ m^{2}s^{-1}, $T_{HAZ} = 995$ °C, T_{max}=$C_m \times T_M$, where $T_M = 1604.85$ °C and $\Delta t = 0.5$ s.

Figures 9 through 23 show estimated transverse cross sections of SZ and HAZ-edge boundaries for Ti-6Al-4V FSWs obtained from experiment (see references [40, 51]) and different two-dimensional slices of three-dimensional temperature fields (°C) calculated using cross section information given in Tables 2, 3 and 4. Values of the workpiece thickness *l* and welding speed *V* for each FSW considered for analysis are given in these figures. The upstream boundary constraints on the temperature field, $T_c = T_{HAZ}$ for (y_c,z_c) defined in Eq. (2), are given in Tables 4, 5 and 6 for the HAZ-edge boundaries.

Given in Tables 7-9 are values of the discrete source function that have been calculated according to the constraint conditions and weld specifications given in Tables 4-6. Specifically, given Tables 4-6 provide target values for objective function minimization, which were obtained by a distributed sampling of estimated HAZ cross sections as measured in the laboratory. The relative location of each discrete source is specified following the procedure for constructing equivalent source distributions, consistent with FSW processes, that is described above.

Shown in figures below are different planer slices of the steady state temperature field that have been calculated according to the constraint conditions given in Tables 4-6 for the estimated HAZ-edge boundary. Referring to the planar slices of the calculated temperature fields shown in these figures, it should be noted that all constraint and boundary conditions are satisfied, namely the condition $T(\hat{x},t) = T_{HAZ} = 995^{o}$C at the HAZ edge, and $\nabla T \cdot \hat{n} = 0$ at surface boundaries, where $\hat{n}$ is normal to the surface. As shown in these figures, the calculated temperature fields have good agreement with experimentally measured cross sections for HAZ-edge boundaries.

Table 4 Estimated SZ-edge and HAZ-edge boundaries on transverse cross section of Weld 3.

SZ

ADVANCING SIDE	RETREATING SIDE
(y_c mm, z_c mm)	*(y_c mm, z_c mm)*
(5.75, 0.25)	(5.625, 0.25)
(5.25, 0.75)	(5.125, 0.75)
(4.5, 1.375)	(4.25, 1.375)
(2.625, 2.0)	(2.625, 2.0)
(2.0, 2.625)	(2.0, 2.625)
(2.0, 3.0)	(2.0, 3.0)

HAZ

ADVANCING SIDE	RETREATING SIDE
(y_c mm, z_c mm)	*(y_c mm, z_c mm)*
(6.818, 0.1364)	(6.682, 0.1364)
(6.682, 0.6818)	(6.682, 0.6818)
(5.000, 2.0000)	(4.375, 2.0000)

Table 5 Estimated SZ-edge and HAZ-edge boundaries on transverse cross section of Weld 4.

SZ

ADVANCING SIDE	RETREATING SIDE
(y_c mm, z_c mm)	*(y_c mm, z_c mm)*
(6.25, 0.25)	(6.5, 0.25)
(5.25, 0.75)	(5.875, 0.75)
(3.75, 1.375)	(4.375, 1.375)
(2.625, 2.0)	(3.125, 2.0)
(2.0, 2.625)	(2.25, 2.625)
(1.375, 3.0)	(1.75, 3.0)

HAZ

ADVANCING SIDE	RETREATING SIDE
(y_c mm, z_c mm)	*(y_c mm, z_c mm)*
(7.363, 0.1364)	(7.363, 0.1364)
(6.682, 0.6818)	(6.954, 0.6818)
(6.136, 1.3636)	(6.000, 1.3636)
(4.910, 2.0454)	(4.636, 2.0454)
(3.545, 2.7272)	(3.136, 2.7272)
(2.182, 3.0000)	(2.454, 3.0000)

Table 6 Estimated SZ-edge and HAZ-edge boundaries on transverse cross section of Weld 5.

SZ

ADVANCING SIDE	RETREATING SIDE
(y_c mm, z_c mm)	*(y_c mm, z_c mm)*
(5.875, 0.25)	(6.125, 0.25)
(5.25, 0.75)	(4.875, 0.75)
(3.25, 1.375)	(3.375, 1.375)
(2.375, 2.0)	(2.5, 2.0)
(2.0, 2.625)	(2.0, 2.625)
(1.625, 3.0)	(1.75, 3.0)

HAZ

ADVANCING SIDE	RETREATING SIDE
(y_c mm, z_c mm)	*(y_c mm, z_c mm)*
(7.363, 0.1364)	(6.954, 0.1364)
(6.818, 0.6818)	(6.545, 0.6818)
(5.454, 1.3636)	(5.863, 1.3636)
(4.091, 2.0454)	(4.500, 2.0454)
(2.727, 2.7272)	(3.136, 2.7272)
(2.182, 3.0000)	(2.318, 3.0000)

Table 7 Source function $C(\hat{x}_k)$ calculated according to HAZ-boundary constraint conditions given in Table 4, where $\gamma = 0.17$, $\Delta l = (3.0/60)$ mm, $x_k = y_k = 0.0$ for $k = 1$ to 4 (Weld 3).

k	$C(\hat{x}_k)/(1.95\text{x}10^{-3})$	z_k (Δl)
1	0.3	10
2	0.57	15
3	0.57	20
4	0.4	25
5	0.4	30

Table 8 Source function $C(\hat{x}_k)$ calculated according to HAZ-boundary constraint conditions given in Table 5, where $\gamma = 0.14$, $\Delta l = (3.0/60)$ mm, $x_k = y_k = 0.0$ for $k = 1$ to 3 (Weld 4).

k	$C(\hat{x}_k)/(4.9\text{x}10^{-3})$	z_k (Δl)
1	0.177	15
2	0.177	20
3	0.174	25

Table 9 Source function $C(\hat{x}_k)$ calculated according to HAZ-boundary constraint conditions given in Table 6, where $\Delta l = (3.0/60)$ mm, $x_k = y_k = 0.0$ for $k = 1$ to 5 (Weld 5).

k	$C(\hat{x}_k)/(2.4\text{x}10^{-3})$	z_k (Δl)
1	0.2	10
2	0.57	15
3	0.57	20
4	0.4	25
5	0.4	30

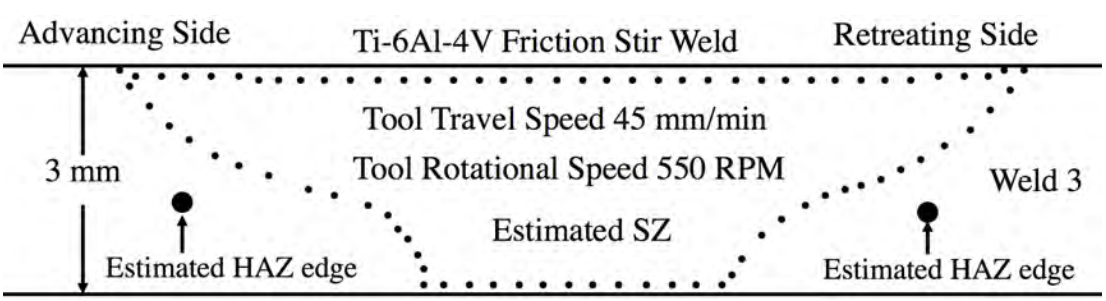

Fig. 9 Experimentally estimated transverse weld cross sections of SZ and HAZ-edge boundaries for Ti-6Al-4V FSW as measured in laboratory [51] (Weld 3).

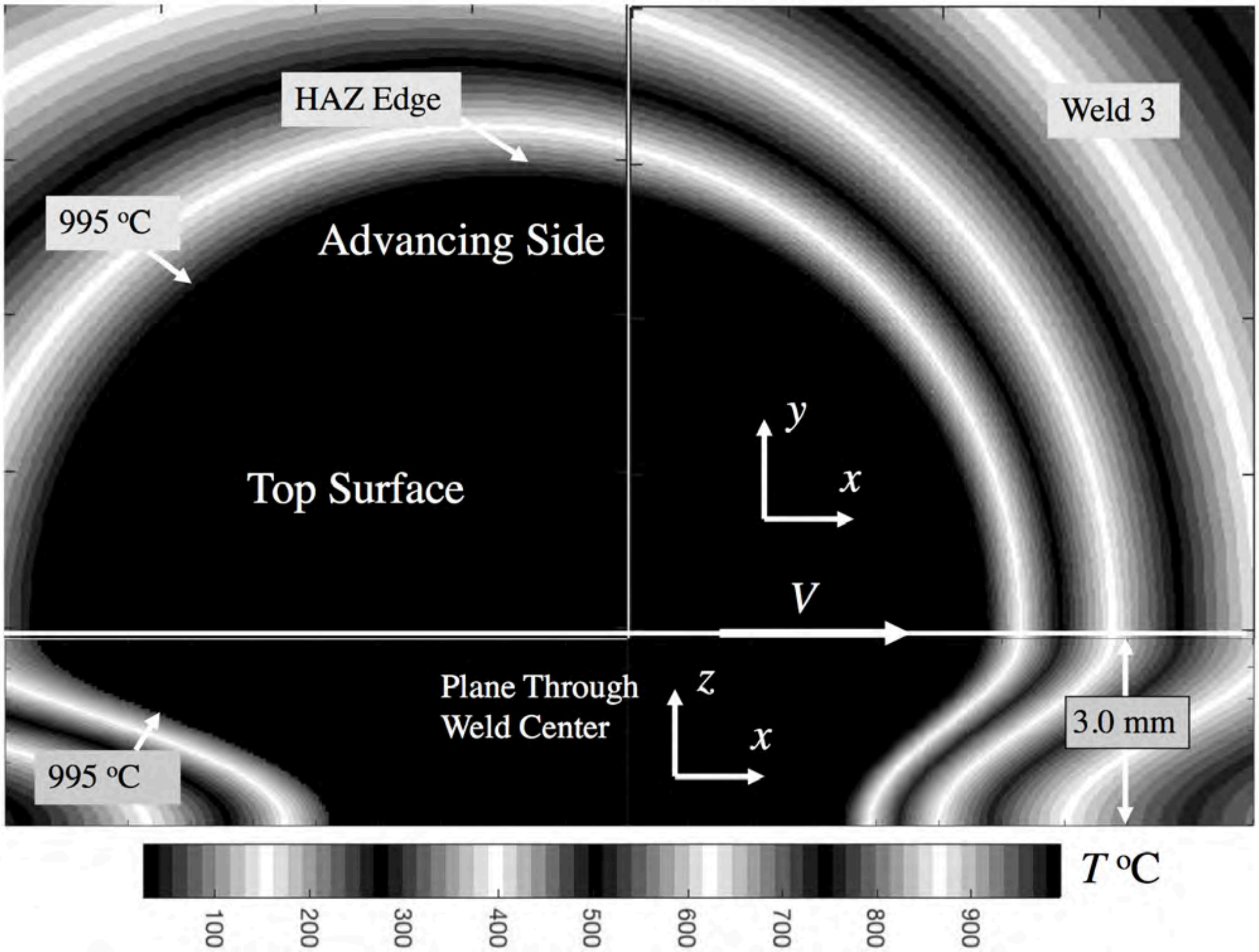

Fig. 10 Two-dimensional slices, at half workpiece top surface and longitudinal cross section at symmetry plane, of three-dimensional temperature field (°C) and isothermal boundary at HAZ edge calculated using cross section information given in Table 4, where time = *x*/V and V = 45 mm/min (Weld 3).

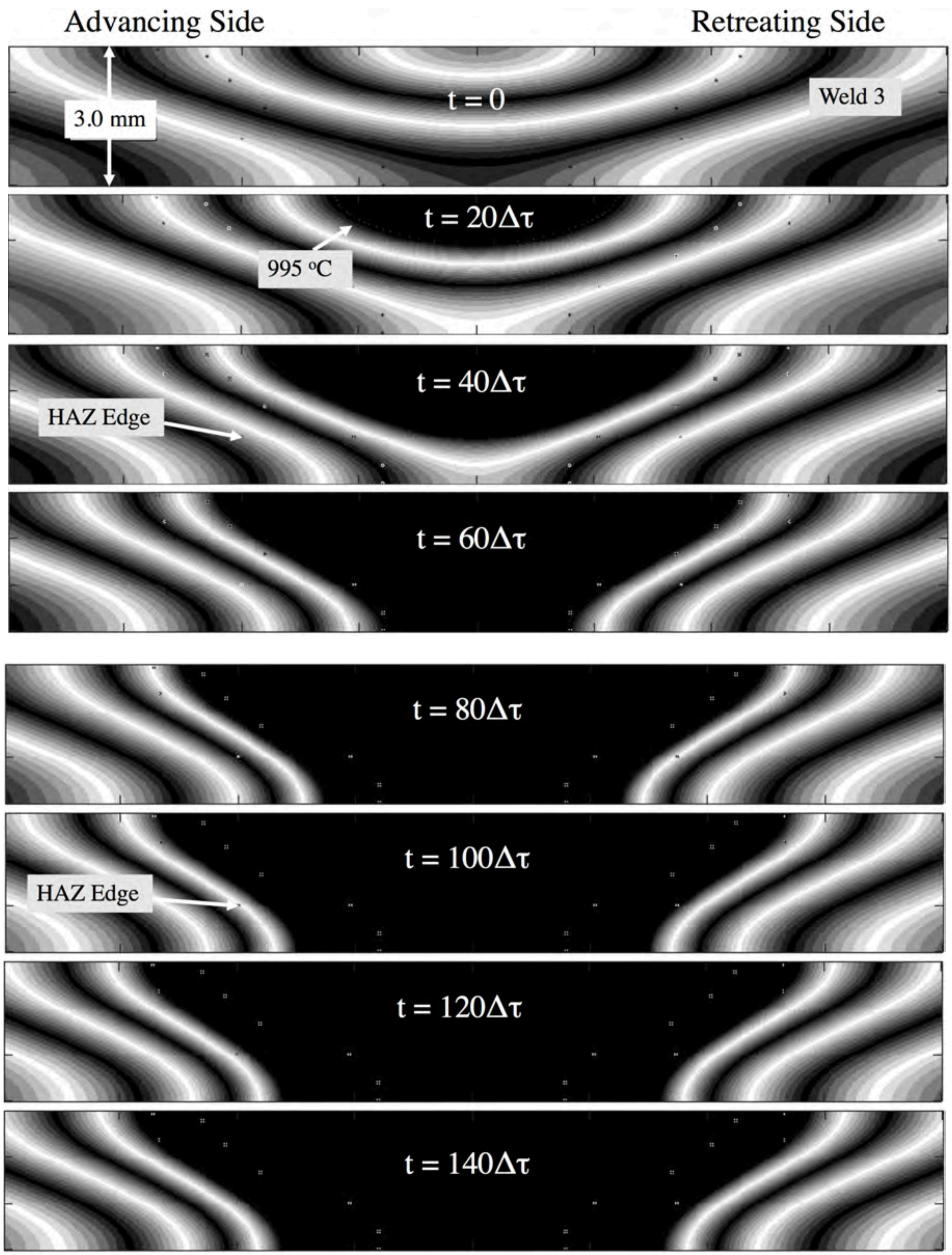
Advancing Side
Retreating Side
3.0 mm
t = 0
Weld 3
t = 20Δτ
995 °C
t = 40Δτ
HAZ Edge
t = 60Δτ
t = 80Δτ
t = 100Δτ
HAZ Edge
t = 120Δτ
t = 140Δτ

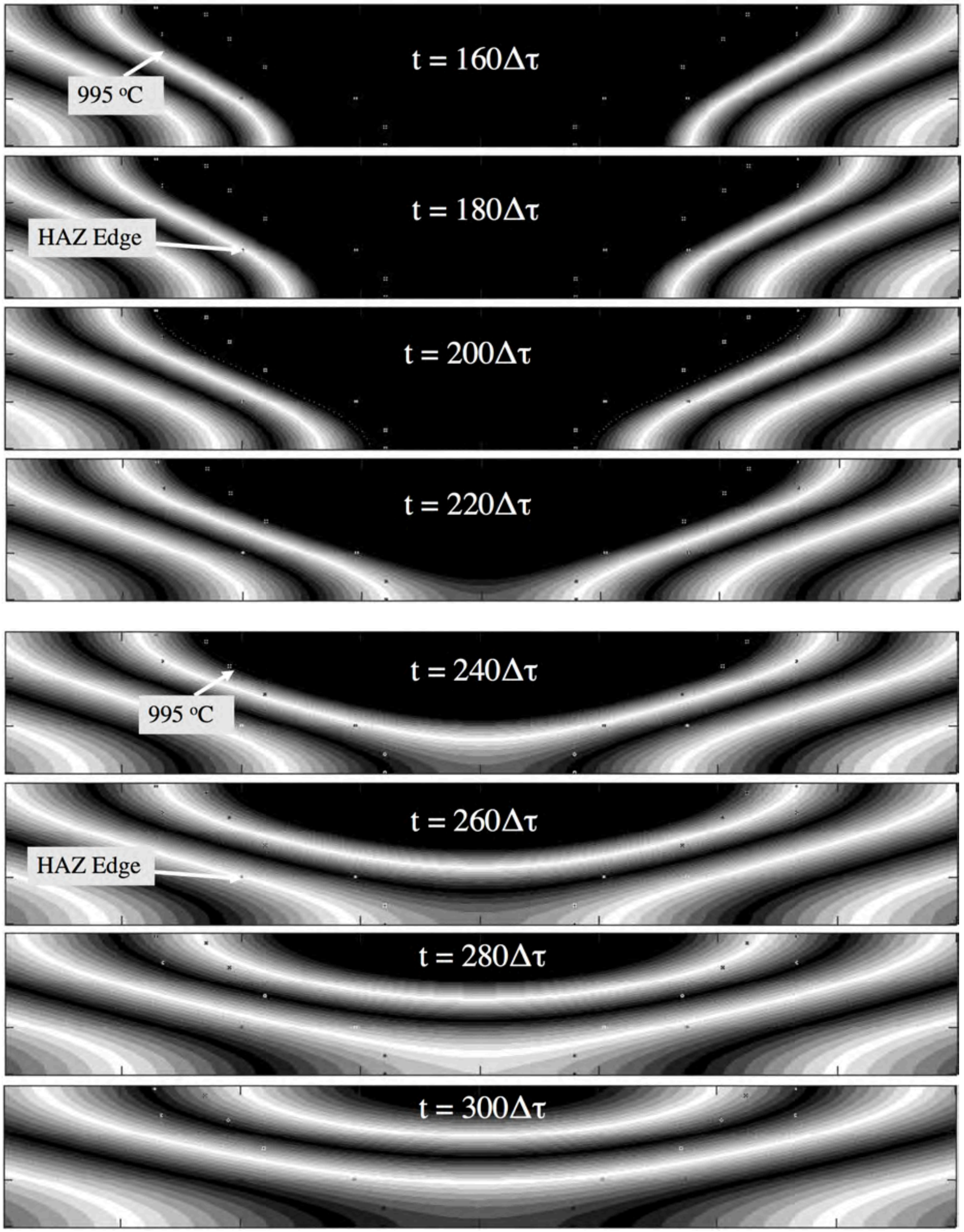

Fig. 11 Temperature history (ºC) of transverse cross section of weld calculated using HAZ cross-section constraints given in Table 4, where $\Delta\tau = \Delta l / V$, Δl = (3.0/60) mm and V = 45 mm/min (Weld 3). Temperature scale shown in Fig. 10.

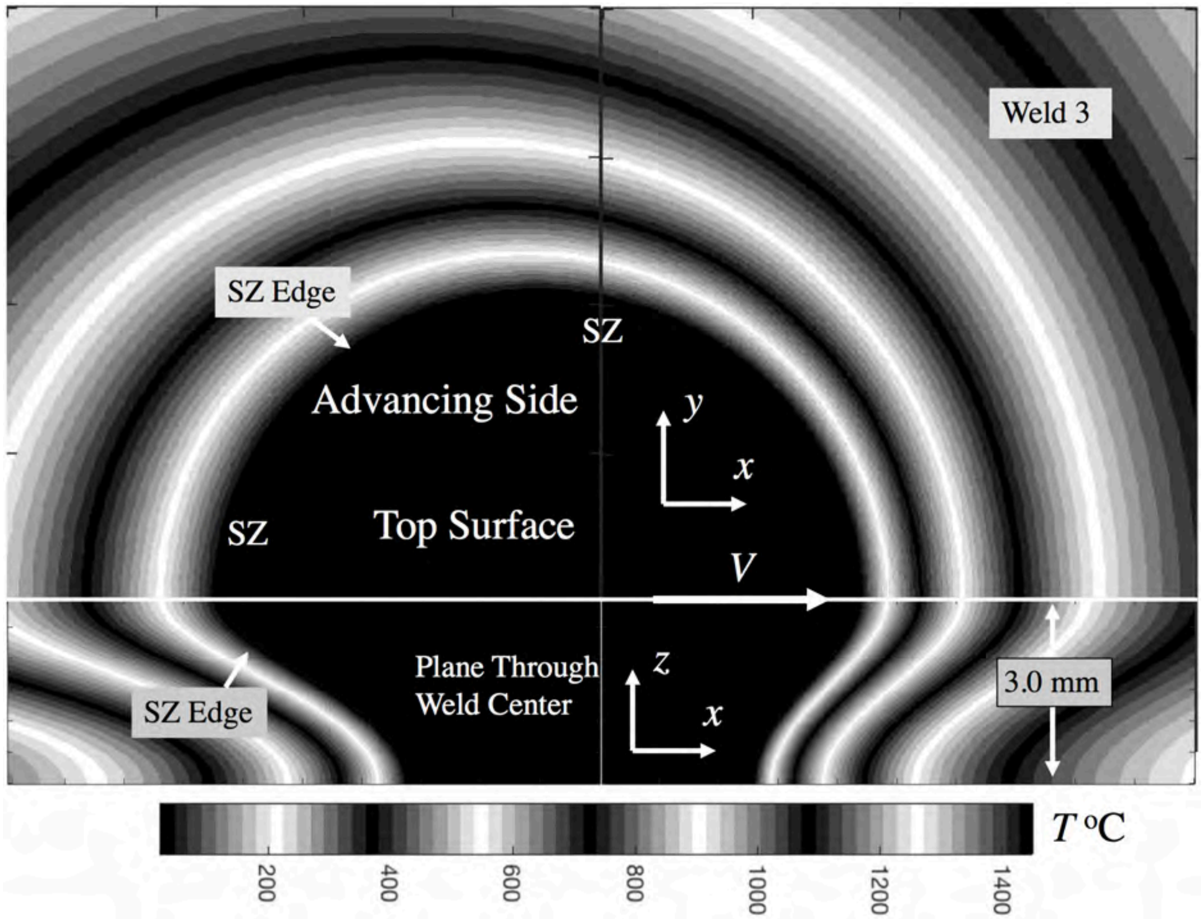

Fig. 12 Two-dimensional slices, at half workpiece top surface and longitudinal cross section at symmetry plane, of three-dimensional temperature field (°C) and isothermal boundary at SZ edge calculated using cross section information given in Table 4, where time = *x*/V and V = 45 mm/min (Weld 3).

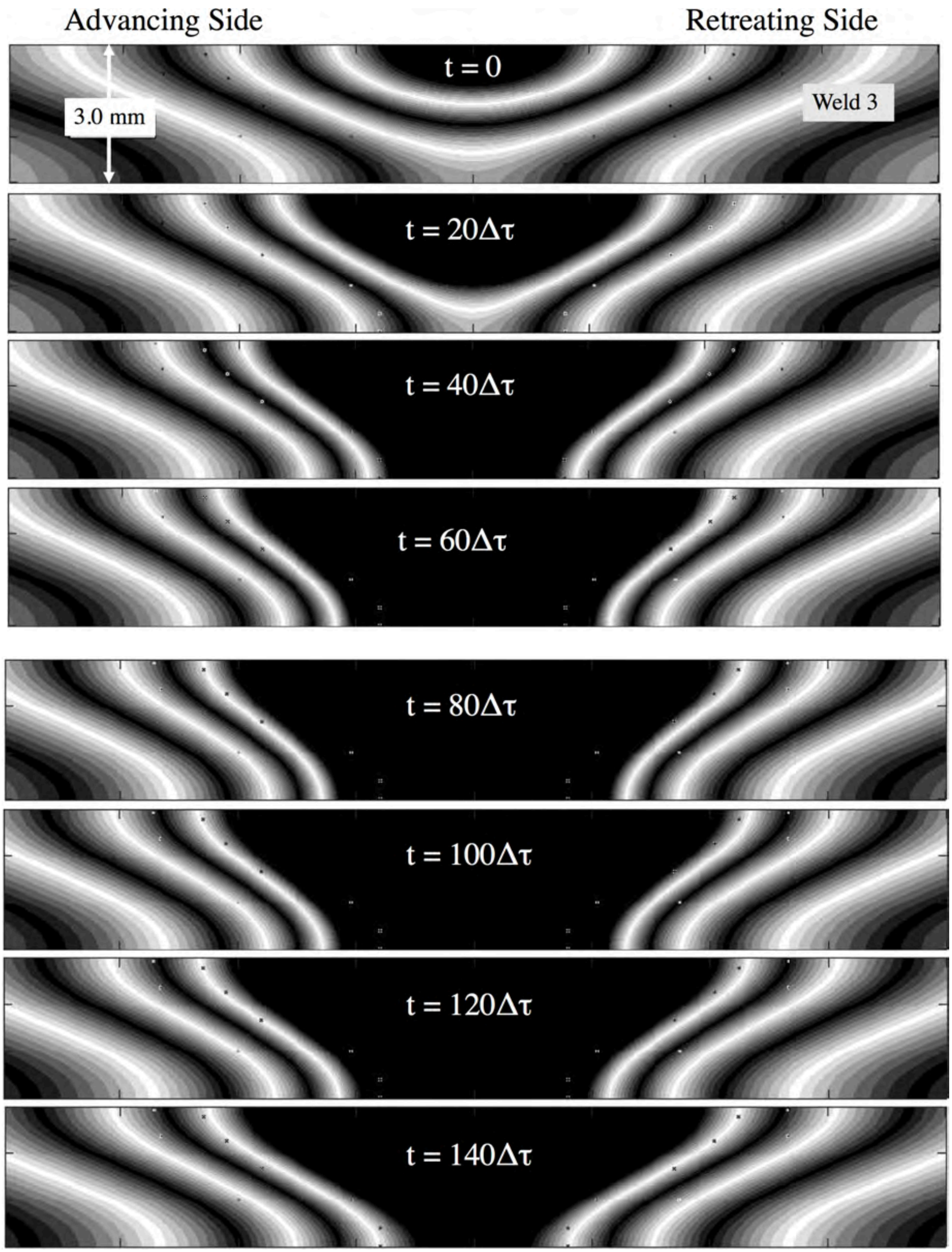
Advancing Side
Retreating Side
t = 0
3.0 mm
Weld 3
t = 20Δτ
t = 40Δτ
t = 60Δτ
t = 80Δτ
t = 100Δτ
t = 120Δτ
t = 140Δτ

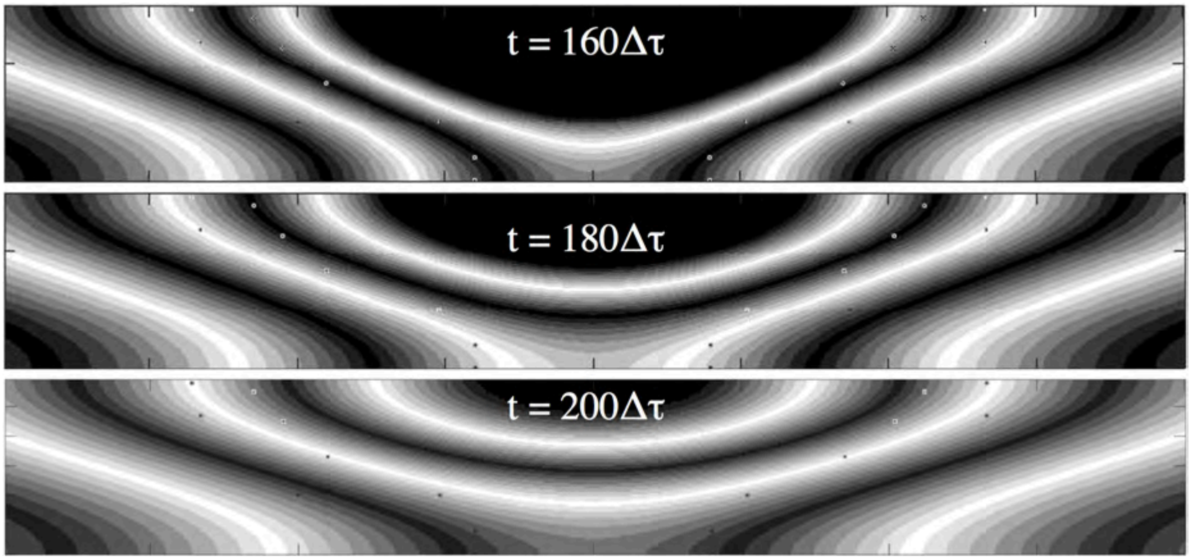

Fig. 13 Temperature history (°C) of transverse cross section of weld calculated using SZ cross-section constraints given in Table 4, where $\Delta\tau = \Delta l / V$, Δl = (3.0/60) mm and V = 45 mm/min (Weld 2). Temperature scale shown in Fig. 12.

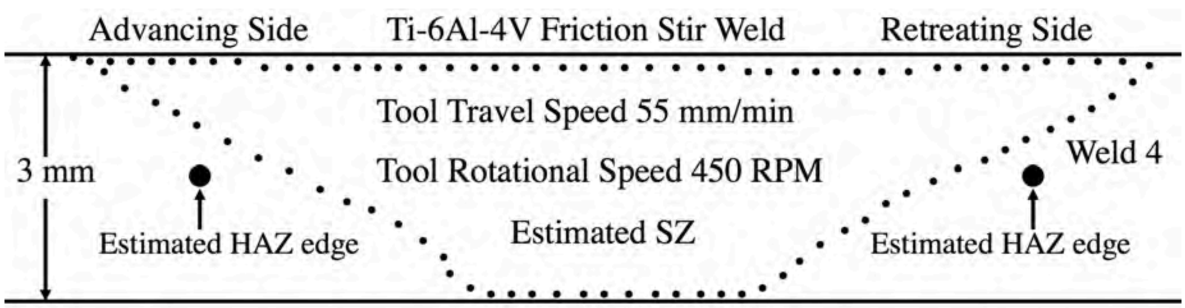

Fig. 14 Experimentally estimated transverse weld cross sections of SZ and HAZ-edge boundaries for Ti-6Al-4V FSW as measured in laboratory [51] (Weld 4).

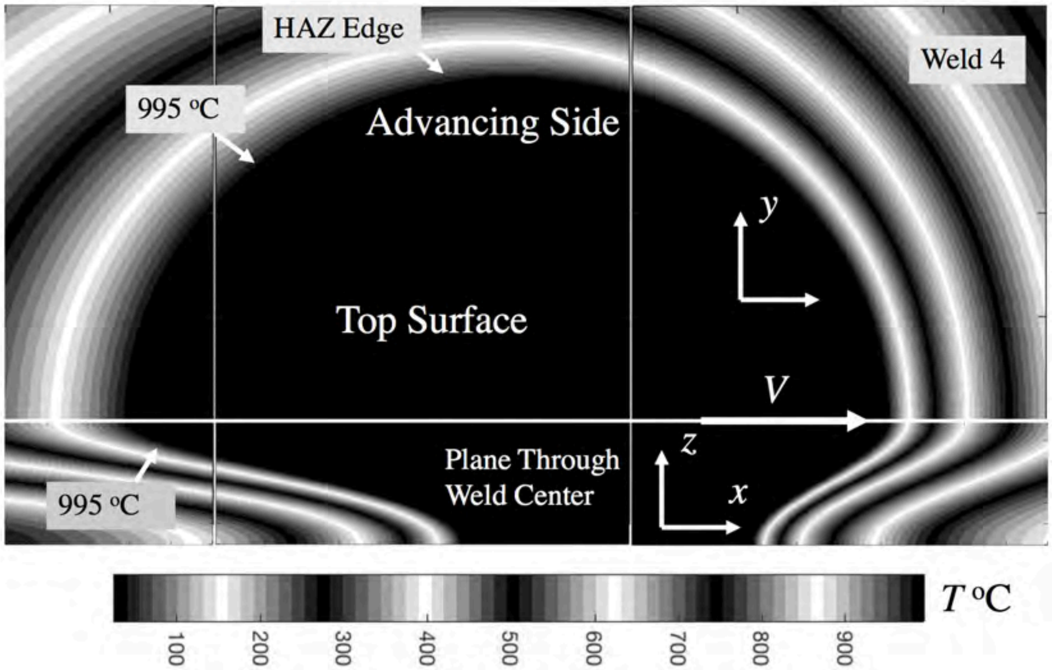

Fig. 15 Two-dimensional slices, at half workpiece top surface and longitudinal cross section at symmetry plane, of three-dimensional temperature field (ºC) and isothermal boundary at HAZ edge calculated using cross section information given in Table 5, where time = *x*/V and V = 55 mm/min (Weld 4).

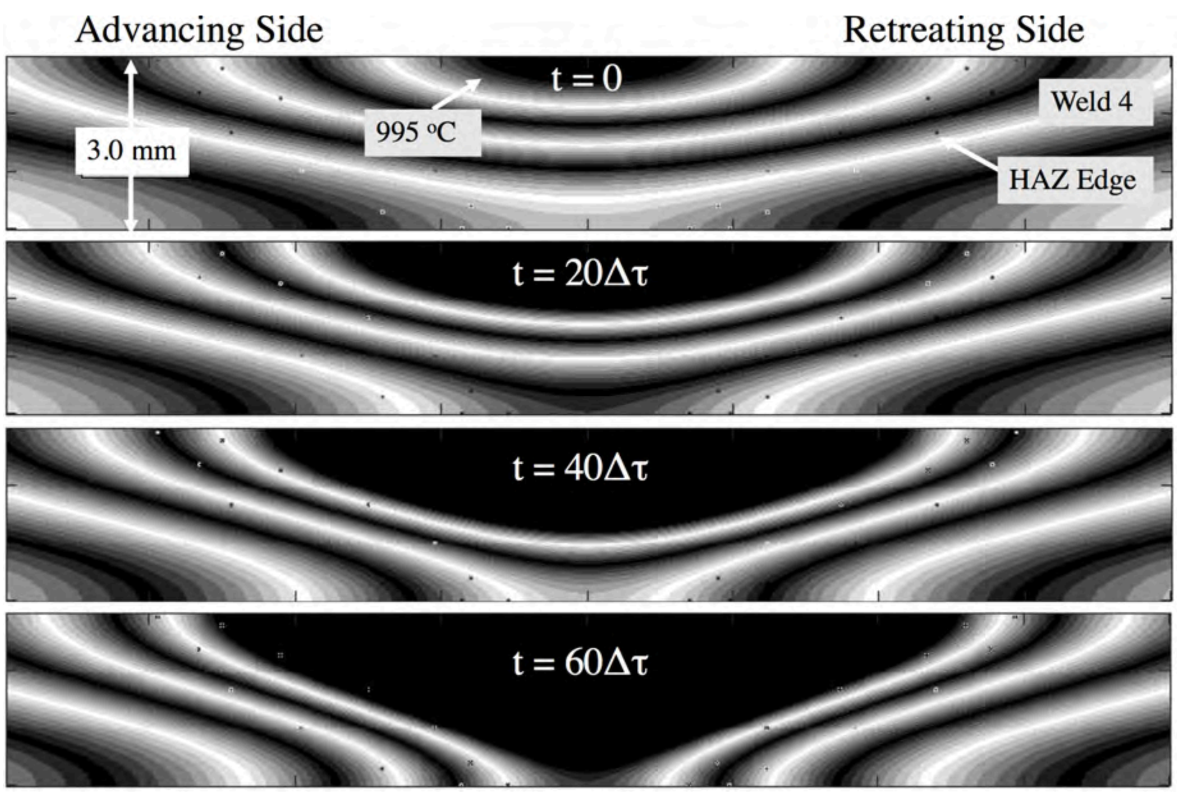

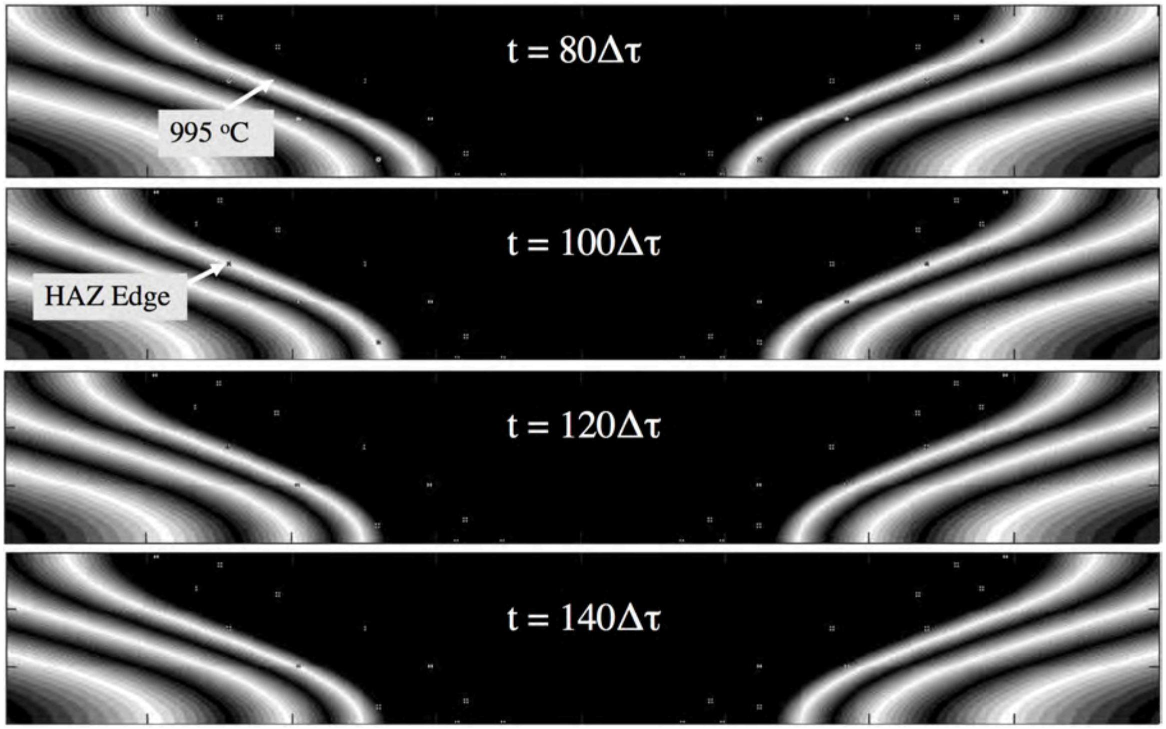
t = 80Δτ
995 °C
t = 100Δτ
HAZ Edge
t = 120Δτ
t = 140Δτ

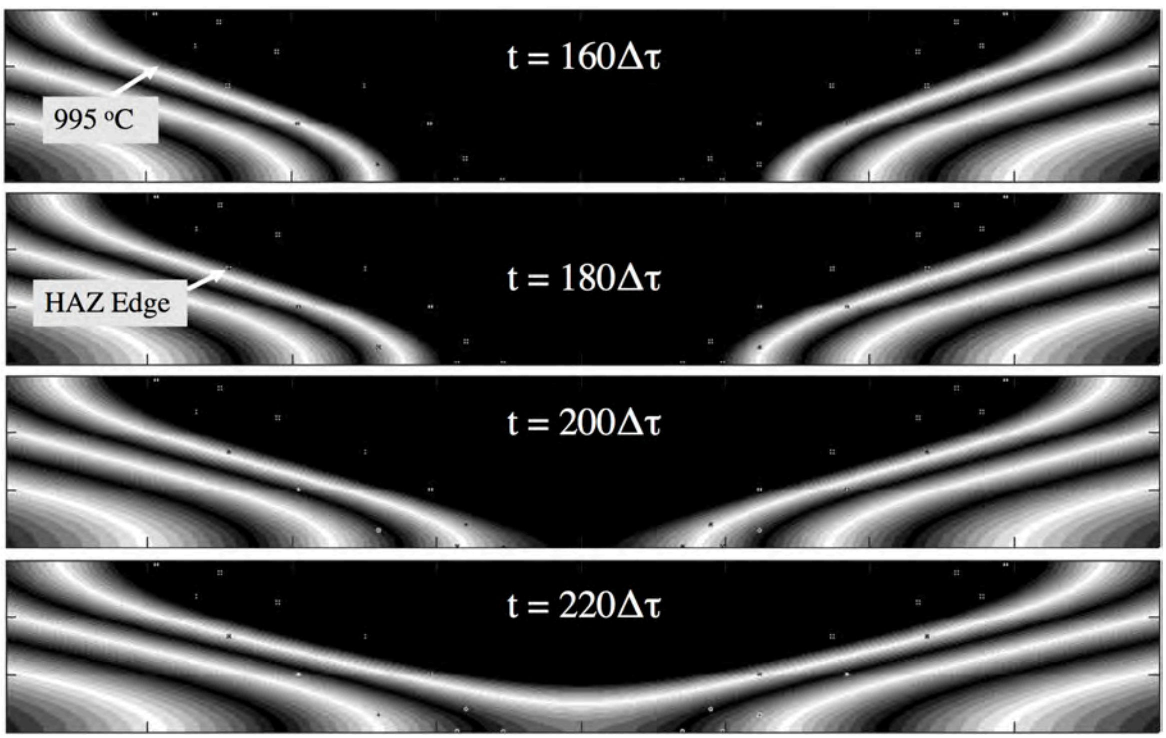
t = 160Δτ
995 °C
t = 180Δτ
HAZ Edge
t = 200Δτ
t = 220Δτ

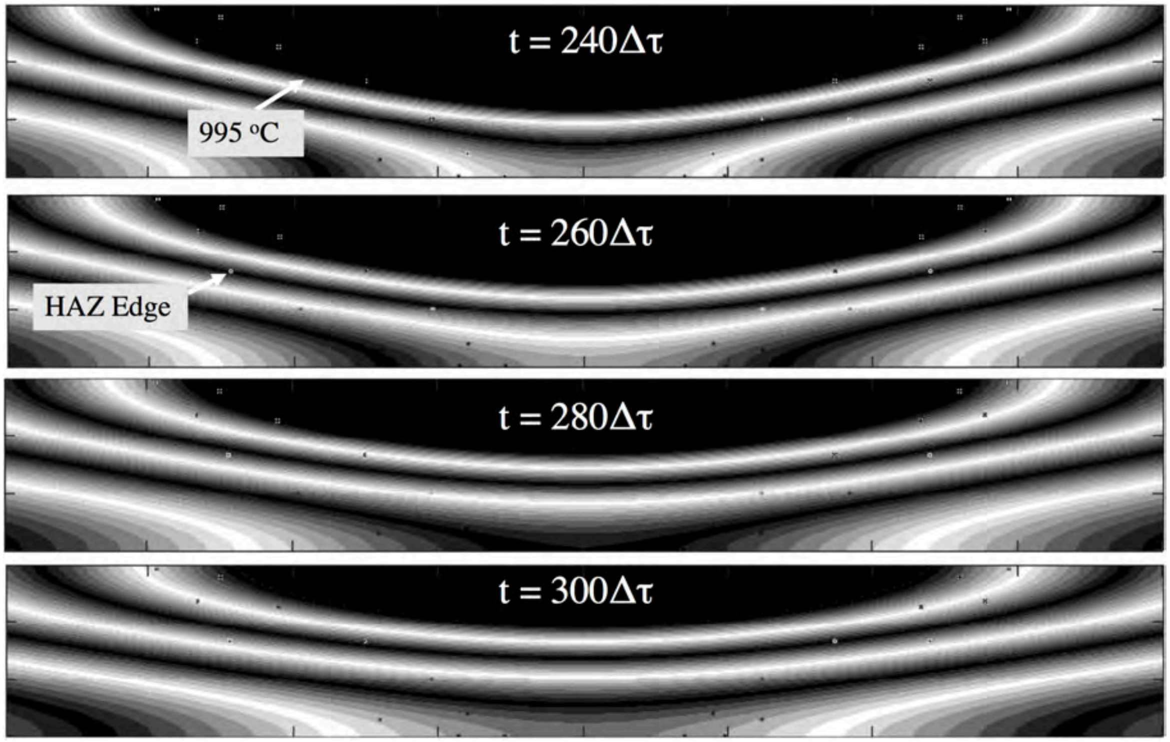

Fig. 16 Temperature history (ºC) of transverse cross section of weld calculated using HAZ cross-section constraints given in Table 5, where $\Delta\tau = \Delta l/V$, Δl = (3.0/60) mm and V = 55 mm/min (Weld 4). Temperature scale shown in Fig. 15.

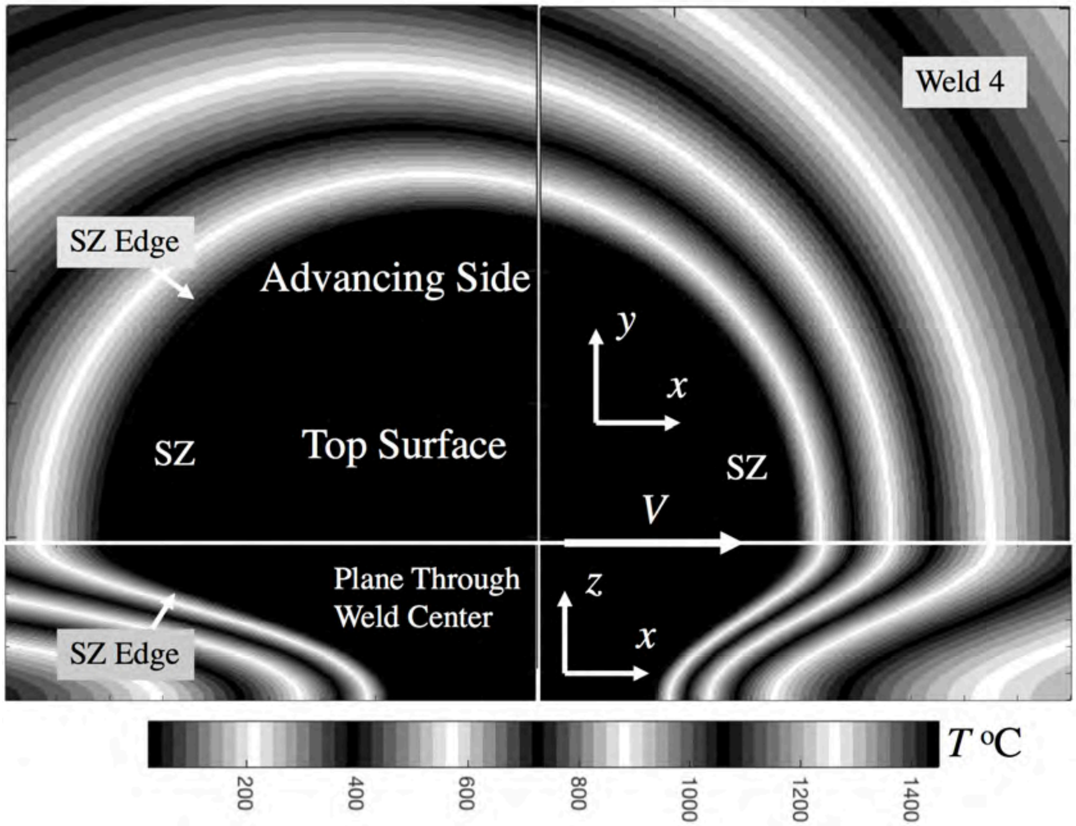

Fig. 17 Two-dimensional slices, at half workpiece top surface and longitudinal cross section at symmetry plane, of three-dimensional temperature field (°C) and isothermal boundary at SZ edge calculated using cross section information given in Table 5, where time = *x*/V and V = 55 mm/min (Weld 4).

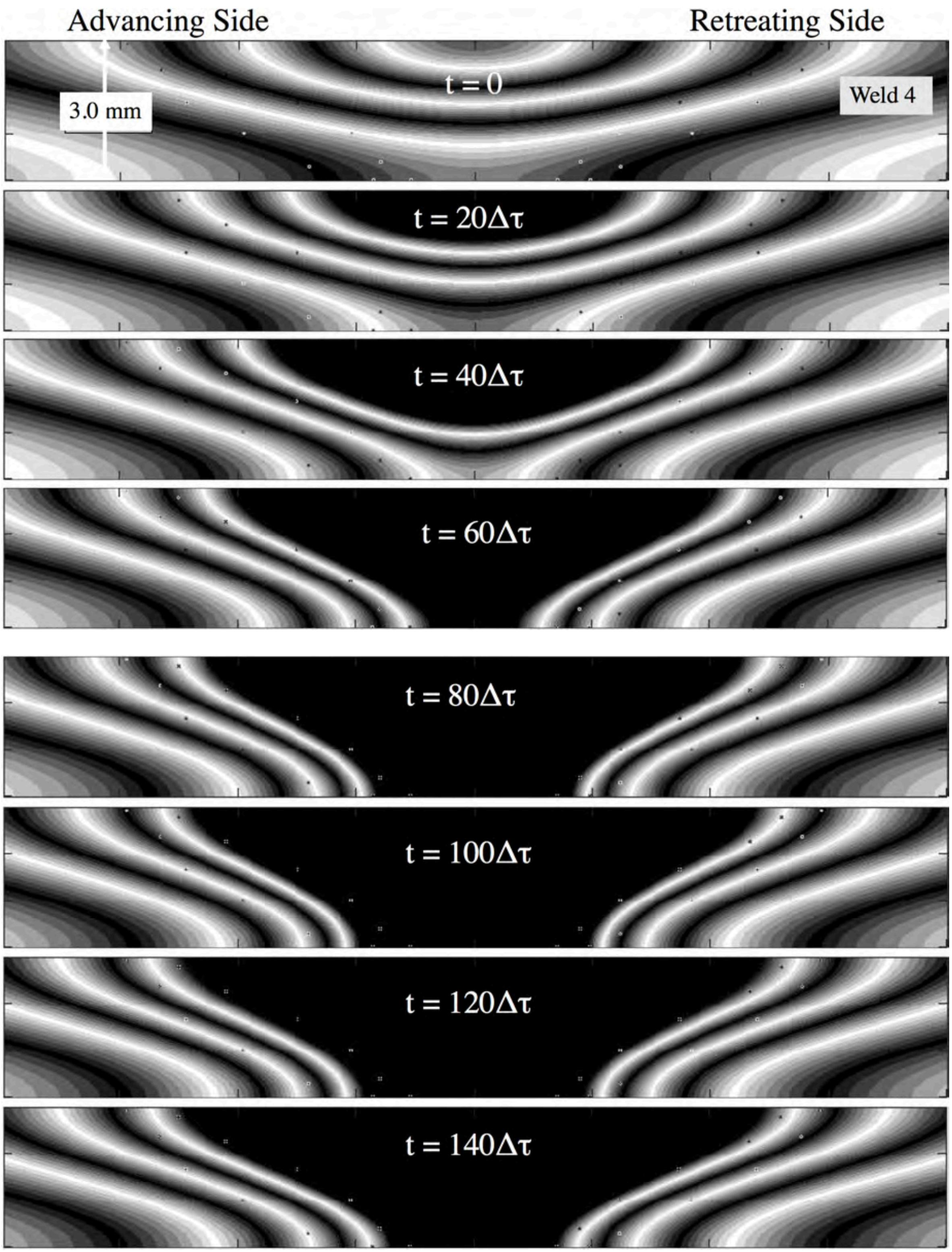
Advancing Side
Retreating Side
3.0 mm
Weld 4
t = 0
t = 20Δτ
t = 40Δτ
t = 60Δτ
t = 80Δτ
t = 100Δτ
t = 120Δτ
t = 140Δτ

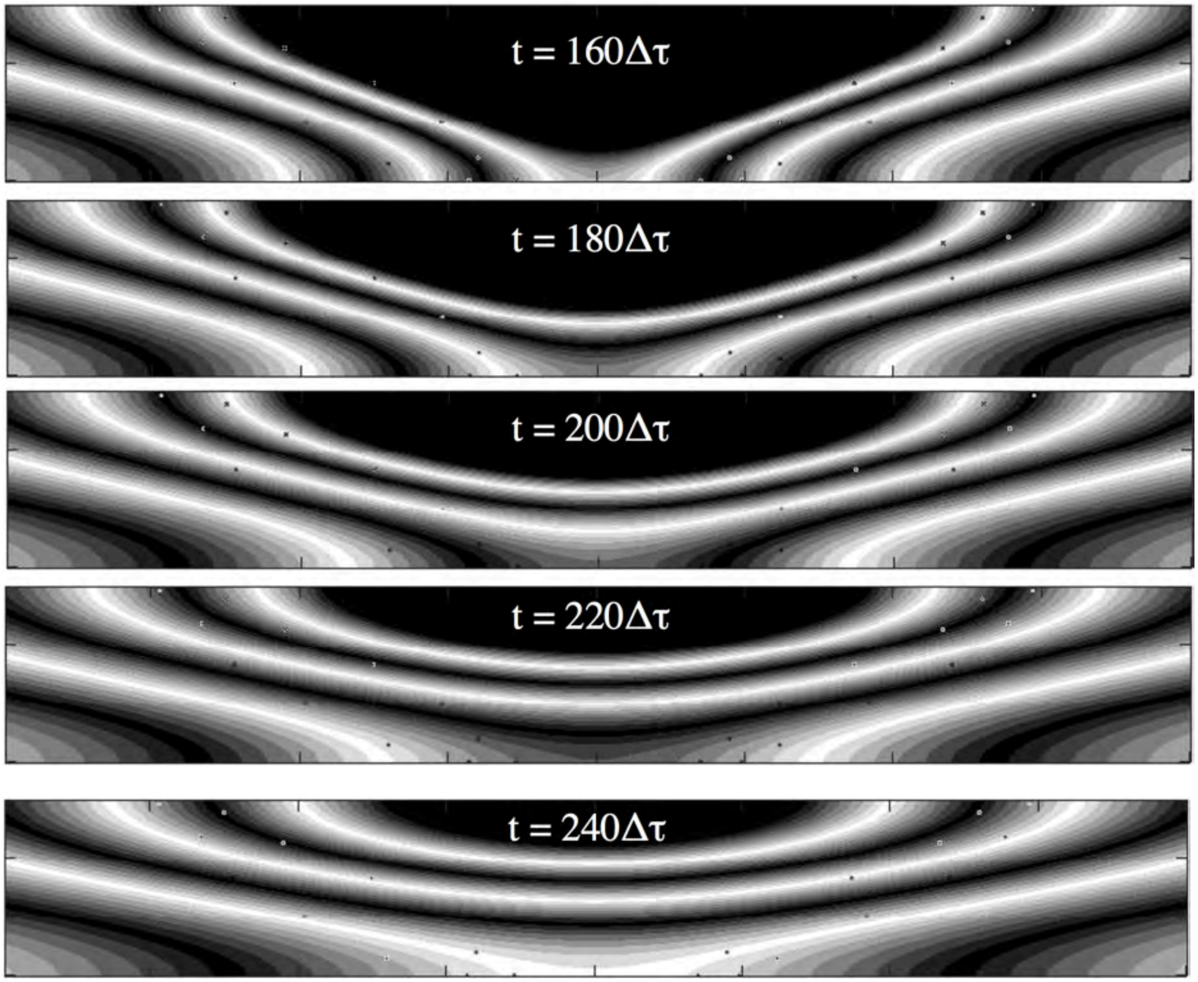

Fig. 18 Temperature history (°C) of transverse cross section of weld calculated using SZ cross-section constraints given in Table 5, where $\Delta\tau = \Delta l / V$, Δl = (3.0/60) mm and V = 55 mm/min (Weld 4). Temperature scale shown in Fig. 17.

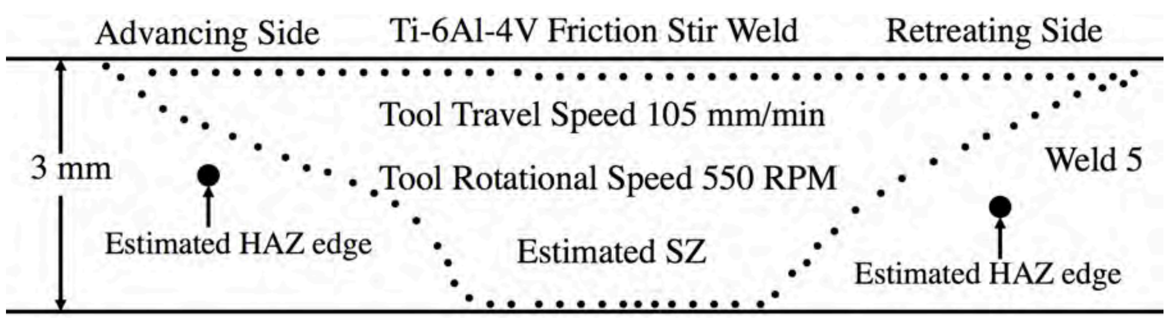

Fig. 19 Experimentally estimated transverse weld cross sections of SZ and HAZ-edge boundaries for Ti-6Al-4V FSW as measured in laboratory [51] (Weld 5).

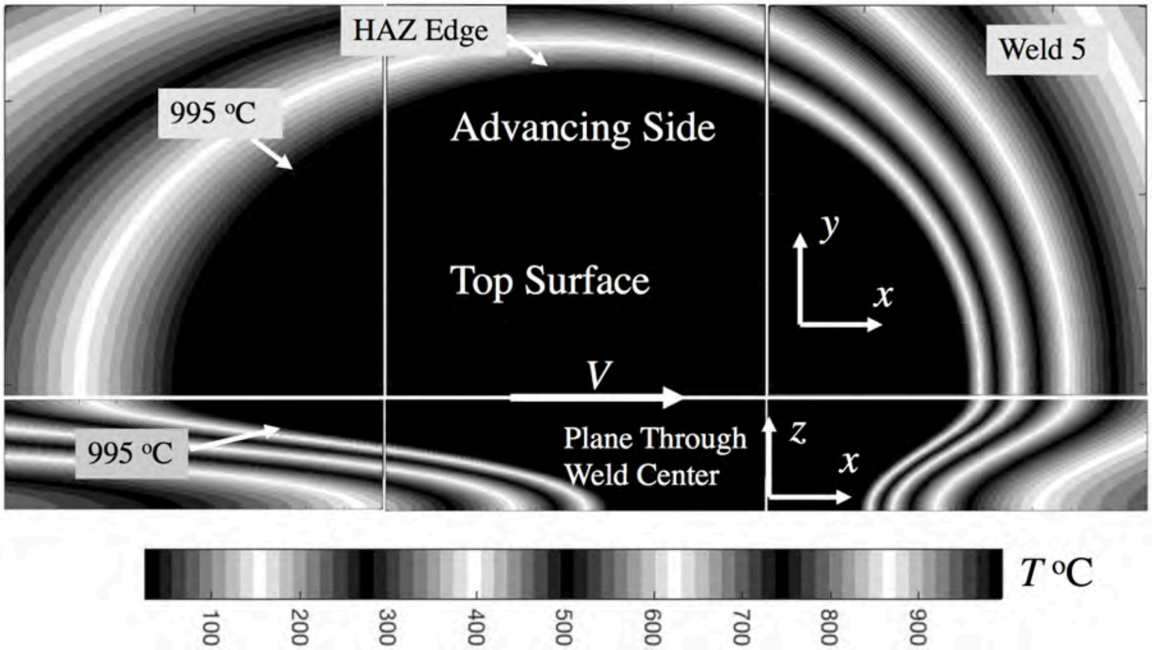

Fig. 20 Two-dimensional slices, at half workpiece top surface and longitudinal cross section at symmetry plane, of three-dimensional temperature field (°C) and isothermal boundary at HAZ edge calculated using cross section information given in Table 6, where time = *x*/V and V = 105 mm/min (Weld 5).

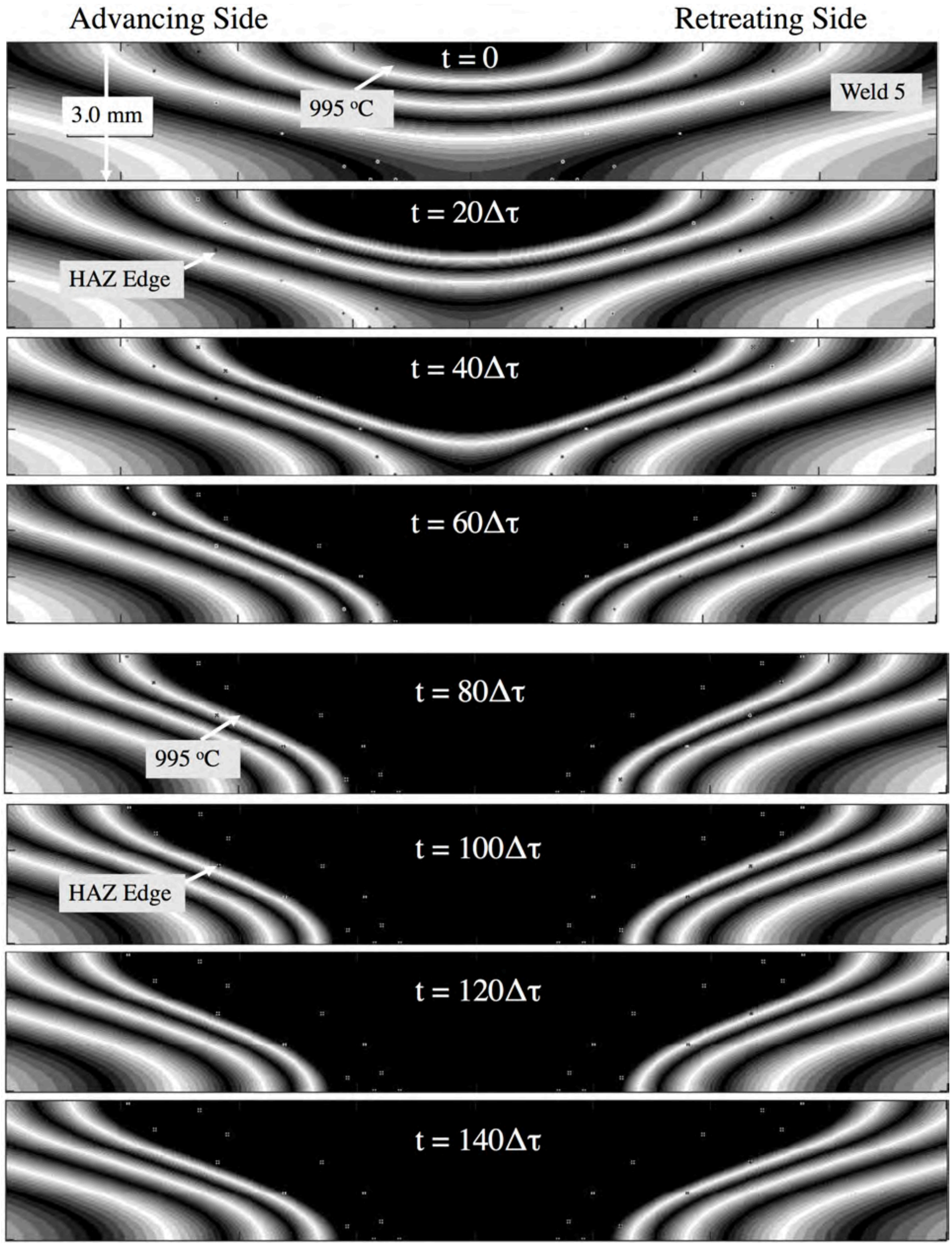
Advancing Side
Retreating Side
t = 0
3.0 mm
995 ºC
Weld 5
t = 20Δτ
HAZ Edge
t = 40Δτ
t = 60Δτ
t = 80Δτ
995 ºC
t = 100Δτ
HAZ Edge
t = 120Δτ
t = 140Δτ

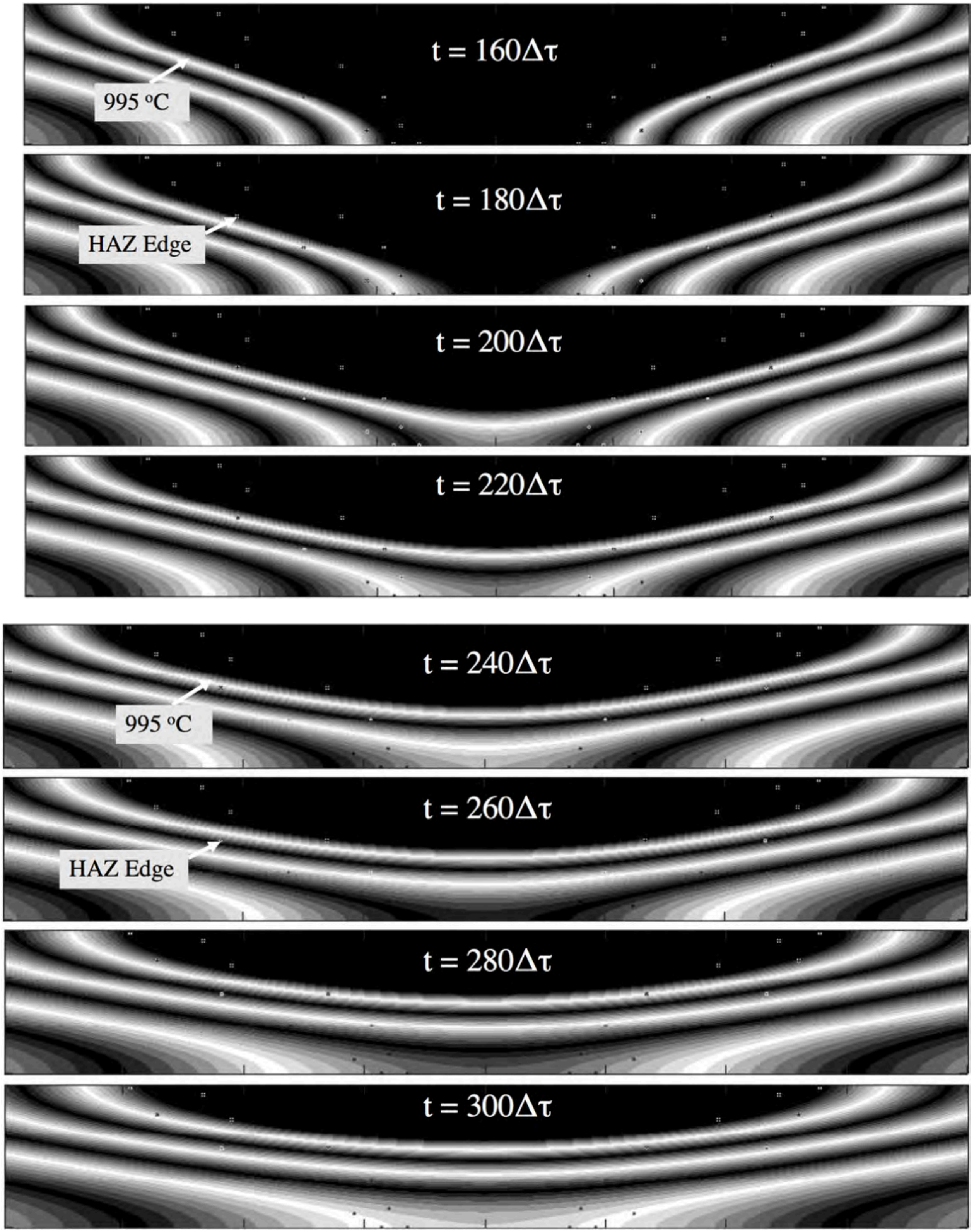
t = 160Δτ
995 ºC
t = 180Δτ
HAZ Edge
t = 200Δτ
t = 220Δτ
t = 240Δτ
995 ºC
t = 260Δτ
HAZ Edge
t = 280Δτ
t = 300Δτ

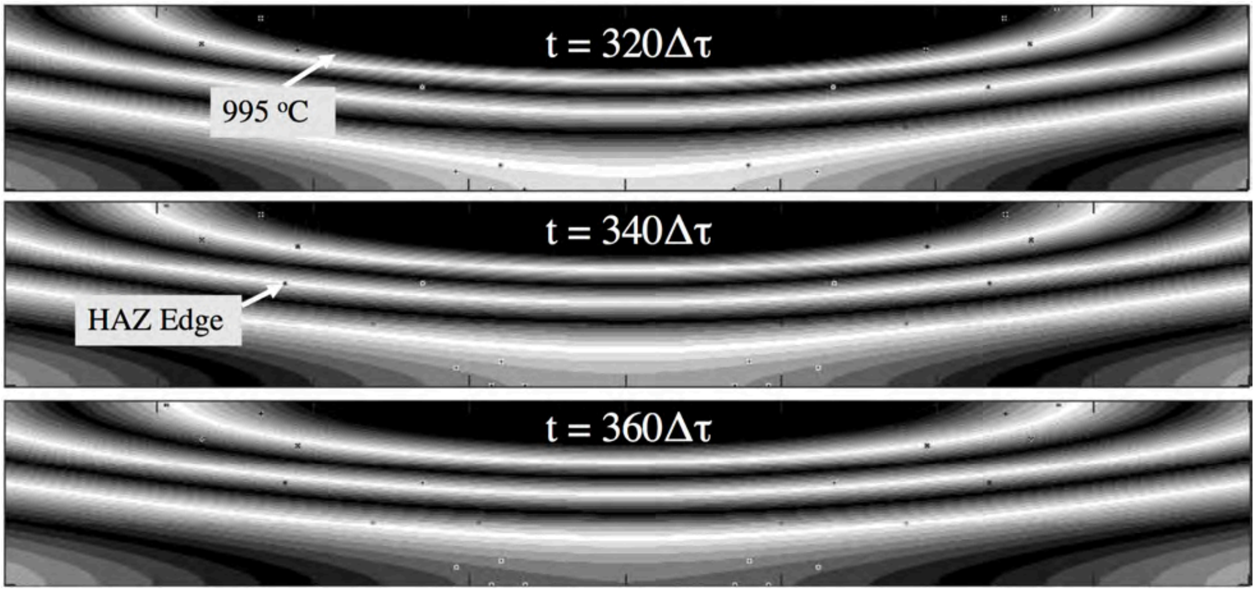

Fig. 21 Two-dimensional slices, at half workpiece top surface and longitudinal cross section at symmetry plane, of three-dimensional temperature field (°C) and isothermal boundary at HAZ edge calculated using cross section information given in Table 6, where time = *x*/V and V = 105 mm/min (Weld 5).

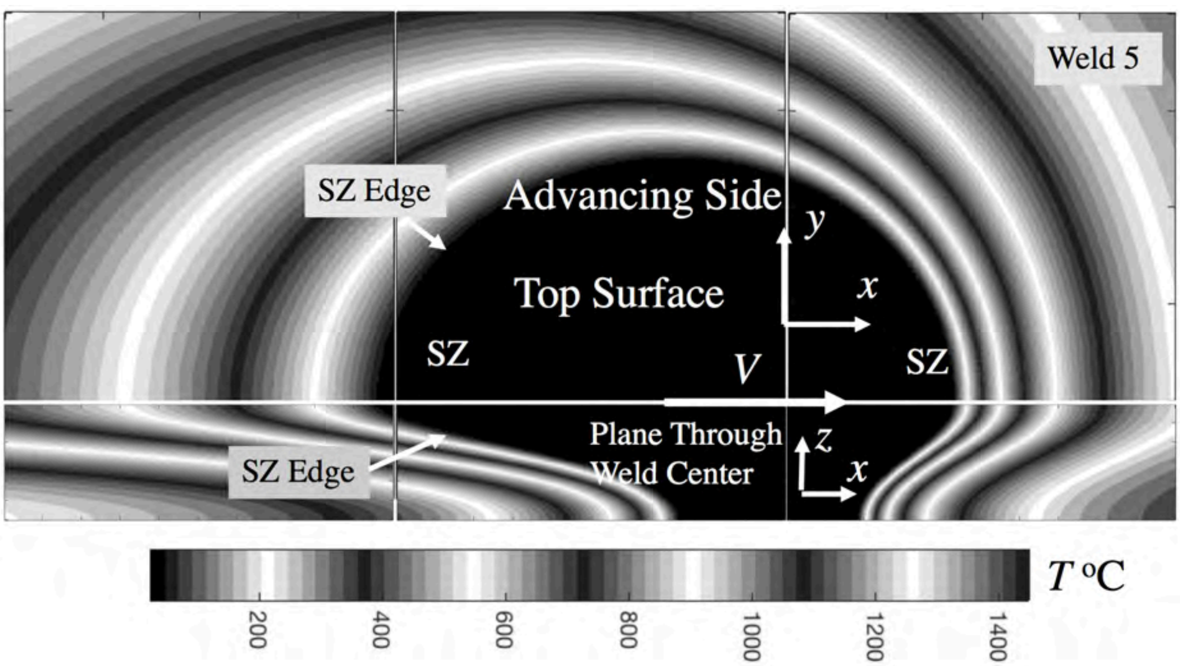

Fig. 22 Two-dimensional slices, at half workpiece top surface and longitudinal cross section at symmetry plane, of three-dimensional temperature field (°C) and isothermal boundary at SZ edge calculated using cross section information given in Table 6, where time = *x*/V and V = 105 mm/min (Weld 5).

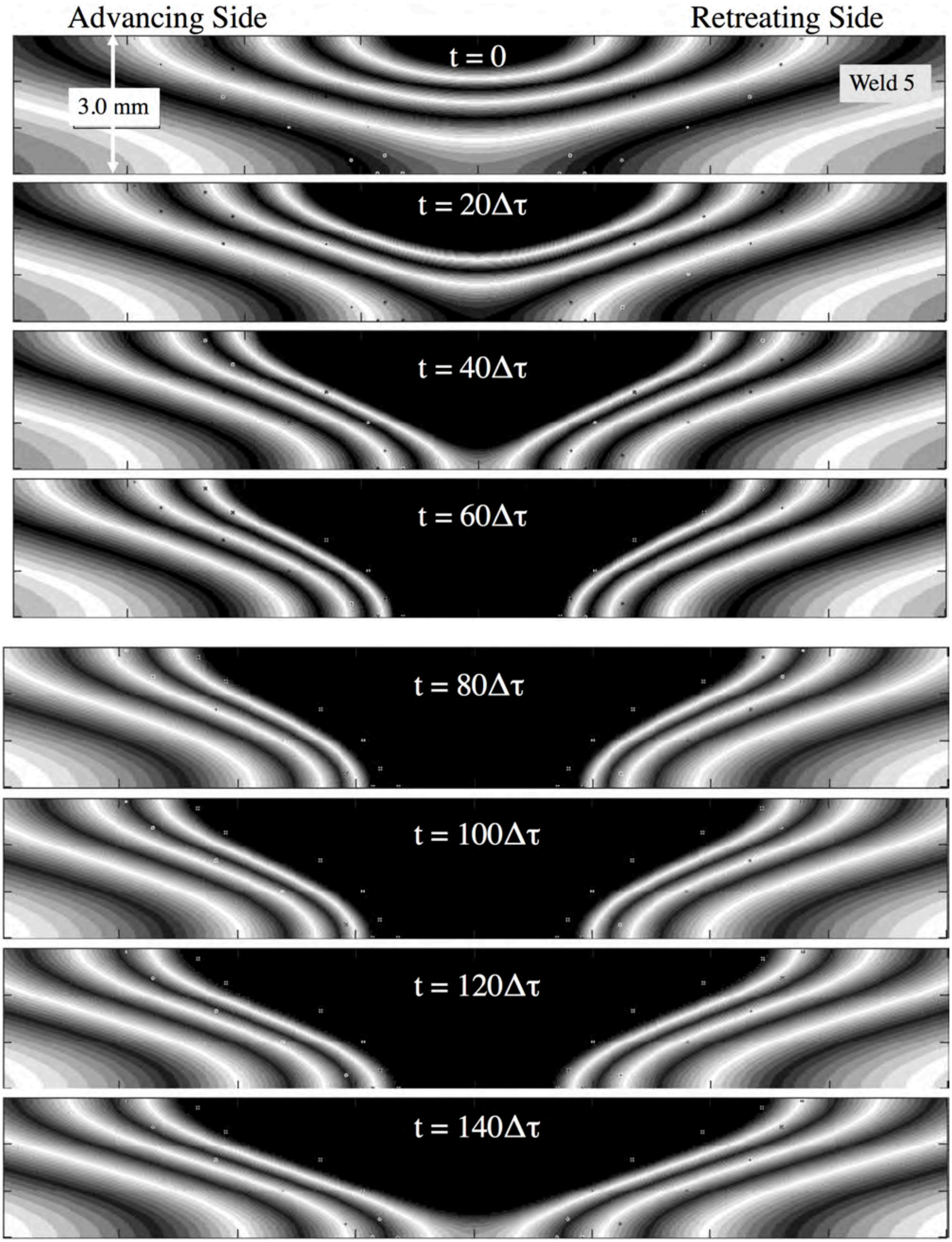
Advancing Side
Retreating Side
t = 0
Weld 5
3.0 mm
t = 20Δτ
t = 40Δτ
t = 60Δτ
t = 80Δτ
t = 100Δτ
t = 120Δτ
t = 140Δτ

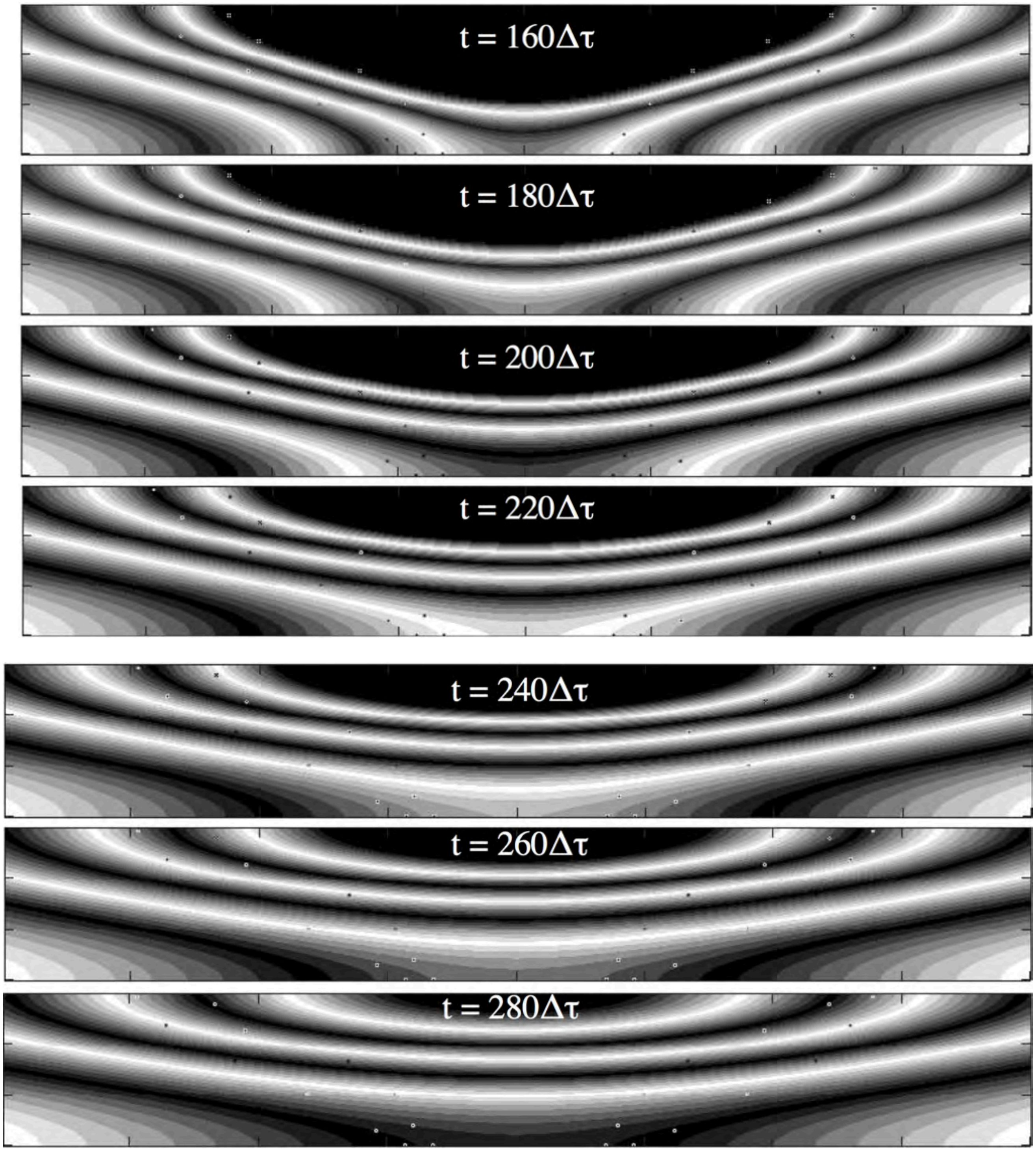

Fig. 23 Two-dimensional slices, at half workpiece top surface and longitudinal cross section at symmetry plane, of three-dimensional temperature field (^oC) and isothermal boundary at SZ edge calculated using cross section information given in Table 6, where time = *x*/V and V = 105 mm/min (Weld 5).

Discussion and Conclusion

The results of this study can be adopted as initial estimates for inverse thermal analysis of other FSWs, i.e., parameter optimization can be made more efficient using initial estimates of parameter values, requiring only fine adjustment with respect to constraint conditions (see [40] and references therein). As for inverse thermal analysis using numerical-analytical basis functions and equivalent source distributions, which have been applied to other types of welding processes [19, 33-36], the parametric temperature histories given here can contribute to a parameter space that contains parameters corresponding to different FSW processes, process conditions and different types of metals and their alloys. As discussed previously [40], adopting estimated SZ-edge or HAZ-edge boundaries as constraint conditions is formally equivalent to using thermocouple measurements for this purpose, i.e, thermocouple measurements can be associated with points on three-dimensional isothermal surfaces. In addition, as discussed previously [40], the parametric FSW temperature fields determined in this study may used for extrapolation of temperature histories from the regions close to the SZ-edge to those within the SZ, and thus provide a means for connecting results of inverse thermal analysis based on parametric modeling, e.g., this study, with those of FSW modeling using basic theory.

Finally, this study demonstrates extension of a methodology for inverse thermal analysis of welds [19, 33-36, 40] with respect to its formulation, which is for application to FSWs. The extension is by inclusion of numerical-analytical basis functions equipped with an effective-duffusity parameterization. Prototype inverse thermal analyses of AZ31-Mg-Alloy and Ti-6Al-4V FSWs are presented that provide proof of concept for inverse thermal analysis using these extended basis functions. This proof of concept is with respect to parameter optimization for different types of SZ shape and HAZ-edge characteristics and boundary conditions.

Acknowledgement

This work was supported by a Naval Research Laboratory (NRL) internal core program.

References

1. Friction Stir Welding and Processing IX, Editors: Y. Hovanski, R. Mishra, Y. Sato, P. Upadhyay and D. Yan, The Minerals, Metals & Materials Series, Springer International Publishing, 2017. DOI: 10.1007/978-3-319-52383-5

2. R.S. Mishra, P.S. De, N. Kumar, Friction Stir Welding and Processing, Science and Engineering, Springer (2014).

3. R. Nandan, T. DebRoy, H.K.D.H. Bhadeshia, "Recent Advances in Fristion-Stir Welding – Process, Weldment Structure and Properties," Progress in Materials Science, 53 (2008), pp. 980-1023.

4. R.K Uyyuru and S. V. Kailas, "Numerical Modeling of Friction Stir Welding Process, Journal of Materials Engineering and Performance, Volume 22(10), 2013, pp. 2013-2921.

5. N. Dialami, M. Chiumenti, M. Cervera, C. Agelet de Saraciber, "An Apropos Kinematic Framework for the Numerical Modeling of Friction Stir Welding," Computers and Structures, 117 (2013), pp. 48-57.

6. M. Chiumenti, M. Cervera, C. Agelet de Saraciber, N. Dialami, "Numerical Modeling of Friction Stir Welding Processes," Comut. Methods Appl. Mech. Engrg. 254 (2013), pp. 353-369.

7. D. M. Neto and P. Neto, "Numerical Modeling of Friction Stir Welding Process: A Literature Review," Int. J. Adv. Manuf. Technol., 65 (2013) pp. 115-126. DOI 10.1007/s00170-012-4154-8.

8. A. Iliopoulos, J.G. Michopoulos, S.G. Lambrakos, "Toward Inverse Estimation of Properties, Process Parameters and Residual Effecyts for Friction Stir Welding," DETC/CIE2015-46532, Proceedings of the ASME 2015 Internatioanl Design Engineering Technical Conference & Computers and Information in Engineering Conference, 2015.

9. M. Song and R. Kovacevic, "Thermal Modeling of Frictions Stir Welding in a Moving Coordinate System and Its Validation, Int. J. of Machine Tools & Manufacture 43 (20030 pp. 605-615.

10. R. Vaira Vignesh, R. Padmanaban, M. Arivarasu, S. Thirumalini, J. Gokulachandran and Mutyala Sesha Sai Ram, "Numerical Modelling of Thermal Phenomenon in Friction Stir Welding of Aluminum Plates," IOP

Conference Series: Materials Science and Engineering, Volume 149, Number 1 (2016) 012208. Doi:10.1088/1757-899X/149/1/012208

11. H.B. Schmidt and J.H. Hattel, “Thermal Modelling of Fristion Stir Welding,” Scripta Materiala 58 (2008), pp. 332-337.

12. P. Heurtier, M.J. Jones, C. Desrayaud, J.H. Driver, F. Montheillet, D. Allehaux, “Mechanical and Thermal Modelling of Friction Stir Welding,” J. of Materials Processing Technology 171 (2006), pp. 348-357.

13. P. A. Colegrove and H.R. Shercliff, “3-Dimensional CFD Modelling of Flow Round a Threaded Fristion Stir Welding Tool Profile,” J. of Materials Processing Technology, 169 (2) (2205), pp. 320-327.

14. P. Ulysse, “Three-Dimensional Modeling of the Friction Stir-Welding Process,” Int. J. of Machine Tools & Manufacture, 42 (2002), pp. 1549-1557.

15. C.M. Chen and R. Kovacevic, “ Finite Element Modeling of Friction Stir Welding – Thermal and Thermomechanical analysis,” Int. J. of Machine Tools & Manufacture 43 (2003), pp. 1319-1326.

16. Y.J. Chao, X. Qi and W. Tang, “Heat Transfer in Friction Stir Welding – Experimental and Numerical Studies,” J. of Manufacturing Science and Engineering, Vol. 125 (2003), pp. 138-145

17. R.W. Fonda and S.G. Lambrakos, “Analysis of Friction Stir Welds using an Inverse-Problem Approach,” Sci. and Tech. of Welding and Joining,” **7** (3) (2002).

18. S.G. Lambrakos, R.W. Fonda, J.O. Milewski and J.E. Mitchell, “Analysis of Friction Stir Welds using Thermocouple Measurements,” Sci. and Tech. of Welding and Joining, **8** 345 (2003).

19. S.G. Lambrakos, “Parametric Modeling of Welding Processes Using Numerical-Analytical Basis Functions and Equivalent Scource Distributions,” Journal of Materials Engineering and Performance, Volume 25(4), 2016, pp. 1360-1375.

20. J.V. Beck, B. Blackwell and C.R. St. Clair, lnverse Heat Conduction: IlI-Posed Problems, Wiley Interscience. New York, 1995.

21. O.M. Alifanov, Inverse Heat Transfer Problems, Springer,Verlag. New York, 1994.

22. M.N. Ozisik and H.R.B. Orlande, Inverse Heat Transfer, Fundamentals and Applications, Taylor and Francis, New York, 2000.

23. K. Kurpisz and A.J. Nowak, Inverse Thermal Problems, Computational Mechanics Publications, Boston, USA, 1995.

24. J.V. Beck, "Inverse Problems in Heat Transfer with Application to Solidification and Welding," Modeling of Casting, Welding and Advanced Solidification Processes V, M. Rappaz, M.R. Ozgu and K.W. Mahin eds., The Minerals, Metals and Materials Society, 1991, pp. 427-437.

25. J.V. Beck, "Inverse Problems in Heat Transfer," Mathematics of Heat Transfer, G.E. Tupholme and A.S. Wood eds., Clarendon Press, (1998), pp. 13-24.

26. A.N. Tikhonov, "Inverse Problems in Heat Conduction," J. Eng. Phys., 29(1), 816-820,1975.

27. O.M. Alifanov, "Solution of an Inverse Problem of Heat-Conduction by Iterative Methods," J. Eng. Phys., 26(4), 471-476, 1974.

28. O.M. Alifanov and V.Y. Mikhailov, "Solution of the Overdetermined Inverse Problem of Thermal Conductivity Involving Inaccurate Data," High Temperature, 23(1), 112-117, 1985.

29. E.A. Artyukhin and A.V. Nenarokomov, "Coefficient Inverse Heat Conduction Problem," J. Eng. Phys.. 53,1085-1090, 1988.

30. T.J. Martin and G.S. Dulikravich, "Inverse Determination of Steady Convective Local Heat Transfer Coefficients," ASME J. Heat Transfer, 120, 328-334, 1998.

31. S.G**.** Lambrakos and S.G. Michopoulos, Algorithms for Inverse Analysis of Heat Deposition Processes, 'Mathematical Modelling of Weld Phenomena,' Volume 8, 847, Published by Verlag der Technischen Universite Graz, Austria (2007).

32. S.G. Lambrakos and J.O. Milewski, Analysis of Welding and Heat Deposition Processes using an Inverse-Problem Approach, Mathematical Modelling of Weld Phenomena, **7**, 1025, Publishied by Verlag der Technischen Universite Graz, Austria 2005, pp. 1025-1055.

33. D. Rosenthal, “The theory of moving sources of heat and its application to metal treatments,” Trans ASME, Vol. 68 (1946), pp. 849-866.

34. J. Goldak, A. Chakravarti and M. Bibby, “A new finite element model for welding heat source,” Metall. Trans. B, Vol. 15, pp. 299-305, 1984.

35. R.O. Myhr and O. Grong,’Acta Metall. Mater., 38, 1990, pp. 449-460.

36. O. Grong, Metallurgical Modelling of Welding, 2ed., Materials Modelling Series, (H.K.D.H. Bhadeshia, ed.), published by The Institute of Materials, UK, (1997), chapter 2: pp. 1-115.

37. S.G. Lambrakos, “Inverse Thermal Analysis of 304L Stainless Steel Laser Welds,” J. Mater. Eng. And Perform., 22(8), 2141 (2013).

38. S.G. Lambrakos, “Inverse Thermal Analysis of Stainless Steel Deep-Penetration Welds Using Volumetric Constraints,” Journal of Materials Engineering and Performance, published online 2014, DOI: 10.1007/s11665-014-1023-7, Volume 23(6), June 2014, pp. 2219-2232.

39. S.G. Lambrakos, “Inverse Thermal Analysis of Welds Using Multiple Constraints and Relaxed Parameter Optimization,” Journal of Materials Engineering and Performance, Volume 24(8) August 2015, pp. 2925-2936.

40. S.G. Lambrakos, “Inverse Thermal Analysis of Ti-6AL-4V Friction Stir Welds Using Numerical-Analytical Basis Functions with Pseuda-Advection,” Journal of Materials Engineering and Performance, published online 2018, DOI 10.1007/s11665-018-3377-8.

41. H. S. Carslaw and J. C. Jaegar: Conduction of Heat in Solids, Clarendon Press, Oxford, 2nd ed, 374, 1959.

42. B.M. Darras, M.K. Khraisheh, F.K. Abu-Farha, M.A. Omar (2007) "Friction stir processing of commercial AZ31 magnesium alloy". Journal of Materials Processing Technology 191, 77–81.

43. Motalleb-nejad P, Saeid T, Heidarzadeh A, Darzi K, Ashjari M (2014) "Effect of tool pin profile on microstructure and mechanical properties of friction stir welded AZ31B magnesium alloy". Mater Des 59:221–226

44. C.I. Chang, C.J. Lee, J.C. Huang (2004) "Relationship between grain size and Zener–Holloman parameter during friction stir processing in AZ31 Mg alloys". Scripta Materialia 51 509–514

45. C.I. Chang, X.H. Du, J.C. Huang, "Producing nano grained microstructure in Mg–Al–Zn alloy by twostep friction stir processing". Scripta Mater., 59, (2008) 356–359.

46. Fang Chai, Datong Zhang and Yuanyuan Li (2014) "Effect of Thermal History on Microstructures and Mechanical Properties of AZ31 Magnesium Alloy Prepared by Friction Stir Processing". Materials, 7, 1573-1589

47. Lorelei Commin, Myriam Dumont, Jean-Eric Masse, Laurent Barrallier (2009) "Friction stir welding of AZ31 magnesium alloy rolled sheets: Inuence of processing parameters". Acta Materialia, Elsevier,57 (2), pp.326-334.

48. Leonardo Contri Campanelli, Uceu Fuad Hasan Suhuddin, Armando Ntalo Sette Antonialli, Jorge Fernandez dos Santos, Nelson Guedes de Alcβntara, Claudemiro Bolfarini (2013) "Metallurgy and mechanical performance of AZ31 magnesium alloy friction spot welds". Journal of Materials Processing Technology 213 515– 521

49. S. Borle, H. Izadi and A.P. Gerlich, “ Influence of Welding Pararmeters on Stir Zone Microstructures During Fricytion Stir Welding of Magnesium Alloys,” The Canadian Journal of Metallurgy and Materials Science, Canadian Metallurgy Quarterly, Vol. 51, No. 3 (2012).

50. S.H. Chowdhury, D.L. Chen, S.D. Bhole, X. Cao and P. Wanjara, “Friction Stir Welded AZ31 Magnesium Alloy: Microstructure, Texture, and Tensile Properties,” Metallurgical and Materials Transactions A, Vol. 44A, 2013, 323-336.

51. P. M. Mashinini, “Process Window for Friction Stir Welding of 3 mm Titanium (Ti-6Al-4V),” Research Dissertation, Magister Technologiae, Mechanical Engineering, 2010 Nelson Mandela Metropolitan University,P.O. Box 77000, Port Elizabeth, South Africa.